

Polarization of stars with debris disks: comparing observations with models

Julien Vandeportal,^{1*} Pierre Bastien,^{1*} Amélie Simon,¹ Jean-Charles Augereau,²
Émilie Storer³

¹Département de physique and Centre de recherche en astrophysique du Québec, Université de Montréal, C.P. 6128, Succ. centre-ville, Montréal, QC H3C 3J7, Canada

²Univ. Grenoble Alpes, CNRS, IPAG, 38000 Grenoble, France

³Department of Physics and Centre de recherche en astrophysique du Québec, McGill University, 3600 University St., Montréal, QC H3A 2T8, Canada

Accepted 2018 October 27. Received 2018 October 12; in original form 2018 July 20

ABSTRACT

The *Herschel* Space telescope carried out an unprecedented survey of nearby stars for debris disks. The dust present in these debris disks scatters and polarizes stellar light in the visible part of the spectrum. We explore what can be learned with aperture polarimetry and detailed radiative transfer modelling about stellar systems with debris disks. We present a polarimetric survey, with measurements from the literature, of candidate stars observed by DEBRIS and DUNES *Herschel* surveys. We perform a statistical analysis of the polarimetric data with the detection of far-infrared excess by *Herschel* and *Spitzer* with a sample of 223 stars. Monte Carlo simulations were performed to determine the effects of various model parameters on the polarization level and find the mass required for detection with current instruments. Eighteen stars were detected with a polarization $0.01 \leq P \leq 0.1$ per cent and $\geq 3\sigma_P$, but only two of them have a debris disk. No statistically significant difference is found between the different groups of stars, with, without, and unknown status for far-infrared excess, and presence of polarization. The simulations show that the integrated polarization is rather small, usually < 0.01 per cent for typical masses detected by their far-infrared excess for hot and most warm disks. Masses observed in cold disks can produce polarization levels above 0.01 per cent since there is usually more dust in them than in closer disks. We list five factors which can explain the observed low-polarization detection rate. Observations with high-precision polarimeters should lead to additional constraints on models of unresolved debris disks.

Key words: circumstellar matter – polarization – scattering – stars: individual (HD 165908, HD 7570, HR 8799, HD 115404) – surveys

1 INTRODUCTION

The first large unbiased survey of debris disks was carried out by the Infra-Red Astronomical Satellite (*IRAS*). It was found that ≈ 15 per cent of main-sequence stars host debris disks (Backman & Paresce 1993; Plets & Vynckier 1999). However, this fraction might be as high as 25 per cent since there is evidence for a population of disks too cold to have been detected by *IRAS* (Wyatt et al. 2003; Lestrade et al. 2006; Rhee et al. 2007). More recently, the DUNES (Eiroa et al. 2013) and DEBRIS (Rodríguez et al. 2015b) *Herschel* surveys measured a fraction of stars with disks as high as 20 ± 2 per cent and 17 ± 2 per cent, respectively. The full DUNES sample of 177 FGK stars within 20 pc was found to have a fraction of 20_{-3}^{+7} per cent (Montesinos et al. 2016) of debris disks. For single

and multiple stars, the rates are 21 ± 3 per cent and 11 ± 3 per cent respectively (Rodríguez et al. 2015a). Marshall et al. (2014) found a fraction of 29 ± 9 per cent debris disks associated with planetary systems, combining the DUNES and DEBRIS samples. Such high proportions of stars hosting debris disks indicate that belts of small bodies (asteroids, comets) are common outcomes of the planet formation process, and survive over long timescales.

Debris disks are found around stars at every age but the lifetime of dust composing them is shorter than that of the hosting star, due to the Poynting–Robertson effect and radiation pressure. However debris disks are still present due to replenishment mechanisms that continuously feed dust to the debris disks (Backman & Paresce 1993). These mechanisms are collisions between planetesimals and sublimation of comets (Williams & Wetherill 1994; Wyatt & Dent 2002; Thébault & Augereau 2007). Hence, observing debris disks is an important way to infer the presence of solid bodies around stars and to understand the dynamics of planetary systems (Wy-

* E-mail: bastien@astro.umontreal.ca (PB) vandeportal.julien@gmail.com (JV)

att 2008; Krivov 2010). Moreover, Beichman et al. (2005) found a correlation between the presence of debris disks and the presence of planets. However, it is still a subject of debate (Kóspál et al. 2009; Maldonado et al. 2015; Marshall et al. 2014). In any case, for spatially-resolved disks, their wide extension and the presence of structures indicates that planetesimals and probably even planets are present and perturb the disk (Backman & Paresce 1993; Ertel et al. 2012; Schneider et al. 2014).

Observing in the close solar environment provides a sample covering a wide range of stellar parameters for which a rich literature already exists. It also maximizes the possibility of finding disks and spatially resolving them. The space telescope *Herschel* observed at far-infrared (FIR) and submillimetre (submm) wavelengths in two of its open time key programs DEBRIS and DUNES. The PACS instrument was used at 70/100 and 160 μm for the surveys, complemented by additional observations with SPIRE at 250, 350 and 500 μm for some selected stars. The DEBRIS targets are the closest evenly distributed stars along the spectral types A, F, G, K and M and constitute a flux-limited survey. The DUNES survey is volume-limited and includes all FGK stars within 20 pc plus a few more out to 25 pc, observed as deep as necessary to detect the stellar photosphere at 100 μm . Since the targets were selected only by their distances, DEBRIS and DUNES samples give us statistical information about debris disks: age, stellar mass, metallicity, presence of planets, system morphology, multiplicity, presence of disks, etc. . . Early results from the DEBRIS survey is given by Matthews et al. (2010) and an exhaustive review by Matthews et al. (2014). Many stars are in common with the James-Clerk-Maxwell Telescope (JCMT) SCUBA-2 Observations of Nearby Stars (SONS) survey at 450 and 850 μm (Phillips et al. (2010, 2012), Matthews et al. (2007), Panić et al. (2013), Holland et al. (2017)). The *Spitzer* telescope with its IRS and MIPS instruments also provided useful data on the short-wavelength side of the *Herschel* coverage, between 7 and 70 μm (Beichman et al. 2006a,b; Gáspár et al. 2013). Hence the spectral coverage spans from 7 to 850 μm for these stars. Distances of the farthest stars are 9, 16, 21, 24 and 46 pc for the M, K, G, F and A stars respectively.

The most efficient way to detect disks in surveys is to use the radiation excess in the infrared (IR) and submm compared to the stellar photospheric flux, as the DUNES (Eiroa et al. 2013) and DEBRIS (Rodríguez et al. 2015b) surveys proceeded. This excess radiation comes from thermal emission by dust grains heated by the star. About half of the *Herschel* disk detections have been resolved (Matthews et al. 2014), and 16 resolved debris disks out of 49 detected disks have been observed by the SONS survey (Holland et al. 2017). The great advantage of resolved observations is the wealth of information available for modelling the disks.

There are other ways to detect debris disks (e.g., Krivov (2010)). With adaptive optics and instruments such as GPI and SPHERE one can image directly the dust in the visible and near-infrared (NIR) but this method is time consuming and is not very efficient for large surveys. One measures stellar light scattered by dust in circumstellar disks which are often resolved for nearby stars (Schneider et al. 2014). Matthews et al. (2014) gave an exhaustive list of resolved disks at various wavelengths.

Polarization is an interesting and useful way to perform surveys because stellar photons scattered by dust into our line of sight are polarized. Such polarization has already been measured in spatially resolved disks such as the β Pictoris (Gledhill et al. 1991; Wolstencroft et al. 1995; Tamura et al. 2006) and the AU Microscopii (Graham et al. 2007) disks. Others such as Oudmaijer et al. (2001); Eritsyan et al. (2002); Tamura & Fukagawa (2005);

Chavero et al. (2006) and Wiktorowicz et al. (2010) presented unresolved polarization measurements of stars with IR excess. Bhatt (1996) and Bhatt & Manoj (2000) compared unresolved polarization of stars with circumstellar matter based on their NIR excess and those that are devoid of such matter. This polarization depends on many properties such as the size, shape and composition of the grains. Even if it is unresolved, polarimetry can also yield the orientation of the disk projected on the plane of the sky, which NIR, FIR or submm excess emission alone cannot provide, unless of course the source is resolved. Two examples of this are given in section 3.1, one observed and the other predicted. Polarization is due to scattering, whose components of the electric field perpendicular and parallel to the scattering plane differ, usually such that the polarization is perpendicular to the scattering plane. This plane includes the light emitter, the scatterer and the observer. The optical thickness in debris disks is so low that multiple scattering is negligible.

In this paper we present a polarimetric survey of 109 stars from the DEBRIS catalogue in section 2. We extend our sample to include measurements in the literature of additional stars from the DUNES & DEBRIS surveys and carry out a statistical analysis of this larger sample in section 3. We present, in section 4, Monte Carlo simulations and use an analytical model to compare with observations. The discussion, in section 5, considers the effects of interstellar polarization, explains why cold disks have larger polarizations and compares with other recent observations. Finally, in the last section we conclude and offer suggestions for future research.

2 OBSERVATIONAL RESULTS

2.1 Observations and other data

The observations were made at the 1.6-m Ritchey-Chrétien telescope of the Mont-Mégantic Observatory (OMM), based in Québec, Canada. We observed in three runs between 2009 December 1 and 2010 March 3. We used an 8.18 arcsec aperture, all multiple stars we observed were integrated at the same time in the 8.18 arcsec aperture. We used a broadband red filter, RG645, which yields a bandpass centered at 766 nm with a FWHM of 241 nm. Polarization was measured with the Beauty and the Beast instrument which is a two-channel photoelectric polarimeter. It uses a Wollaston prism as analyzer, a Pockels cell operated at 125 Hz as modulator, and an achromatic quarter wave plate.

The data were calibrated for polarization efficiency with a prism (between 75 per cent and 83 per cent), for instrumental polarization using unpolarized standards and for the zero point of position angles using polarized standard stars. More information about the instrument and the method of observation is given by Manset & Bastien (1995). We observed unpolarized standards for each run and used the same ones as PlanetPol (Lucas et al. 2009) whenever possible. The polarized standards we observed come from Turnshek et al. (1990) and from the PlanetPol list of polarized stars (Hough et al. 2006).

We adjusted the integration time according to the magnitude of the star in order to have an expected polarization uncertainty of ≈ 0.04 per cent. Uncertainties σ_P are calculated with photon statistics and also include the previous uncertainty due to calibration mentioned above. The uncertainties range between 0.02 per cent and 0.12 per cent (with a mean of 0.04 per cent). The uncertainty on the polarization position angles (hereafter polarization angles)

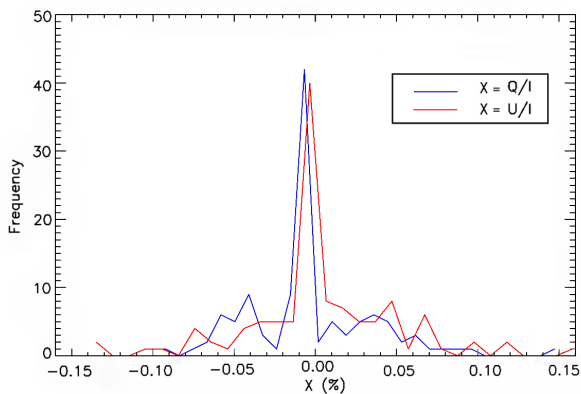


Figure 1. Frequency distribution of the normalized Stokes parameters Q/I and U/I for all stars measured at OMM.

are computed as usual (Serkowski 1962) with

$$\sigma_{\theta} = 28.65^{\circ} \frac{\sigma_P}{P}. \quad (1)$$

The data were pre-analysed by the computer ‘the Beauty’ while observing. The rest of the analysis was automated using IDL programs created for this purpose. The data were also corrected for bias in the usual way (Serkowski 1962). We assumed that circular polarization would be negligible when we did the data reduction. Of the 297 DEBRIS stars that are visible from the observatory 108 were observed for this analysis. We also observed the star HR 8799 even if it is not included in the DEBRIS survey, as it is a target of particular interest: it hosts four imaged planets (Marois et al. 2008, 2010) and debris disks (Su et al. 2009; Reidemeister et al. 2009).

2.2 Results

All targets from the DEBRIS and DUNES surveys are nearby stars with the furthest one at 46 pc. In our analysis we assume that the interstellar polarization is negligible for such distances (Piirola 1977; Korhonen & Reiz 1986; Leroy 1993a; Lucas et al. 2009); hence the polarization we measured is intrinsic to the stars (see the discussion in section 5.1 for more information).

The instrument works in such a way that there is a redundancy in the measurements of the Stokes parameters: measurements were taken at 0° , 45° , 90° and 135° from a certain reference. Hence measurements at 0° and 90° for example should give approximately the same results. We compared the data between 0° and 90° and between 45° and 135° , for all measurements above $2\sigma_P$. We found that measurements are coherent, but not strongly correlated.

We plot the histograms of stars with a given Q/I and U/I in Figure 1. Firstly, we can verify that the instrumental polarization is well determined; in this case we should have a peak in the distributions around 0 per cent. We see that it is the case for U/I but Q/I has a small offset of -0.01 per cent. It is nonetheless smaller than the uncertainty on the determination of the instrumental polarization, therefore it is compatible with 0 per cent. A very strong peak around 0 per cent is seen in both distributions, with two bumps around that peak. This indicates that the uncertainties were larger on certain nights than on others. It is indeed the case as we had some problems with one of the two photomultipliers during some nights and we had to use only half of the data. Finally, we cannot clearly conclude about the presence of polarized stars which would stand in the wings of the peaks. Results are given in Tables 1 and

A1 (Appendix A) and are presented with the full sample in section 3.

2.3 HR 8799

We observed also HR 8799 even if it is not a target of the DEBRIS survey. We found a small polarization of 0.07 per cent at 2.8 times the uncertainty (Table A1). This star is particularly interesting since it hosts four resolved planets (Marois et al. 2008, 2010). Su et al. (2009) and Reidemeister et al. (2009) modelled the IR/submm excess of HR 8799 and found that this star also hosts three debris disks: an inner warm disk, a planetesimal disk and a halo. Confirmation of our 2.8σ result and observations in other wavelength bands would provide better constraints on the debris disks.

2.4 Discussion

We have made a coherent census of the polarization due to debris disks for 109 stars. We have one detection above $3\sigma_P$ (HD 115404 = K046) which is what one should expect statistically for such a sample. This rate can be explained by many factors: only ≈ 17 per cent of DEBRIS survey stars were found to have debris disks (Rodríguez et al. 2015b); in face-on disks the integrated polarization vector cancels out by symmetry (only a fraction of disks have favourable inclinations for detection) and we have measurement uncertainties of ≈ 0.04 per cent, which seems to be at the limit of detection (see section 4). The case of an eccentric disk is considered in the simulations presented below (section 4). More importantly, since we used an 8.18 arcsec aperture centered on the star the unpolarized light from the star is integrated at the same time as the polarized light from the disk. This dilution decreases very significantly the polarization detected. For example β Pictoris has been found to be 15 per cent polarized when the star is hidden (Gledhill et al. 1991) but through a whole aperture, the intrinsic polarization was measured to be only 0.2 per cent (Krivova et al. 2000). Hence, we might overlook debris disks if the mean polarization uncertainty in our survey is too high. In order to push forward and have better statistics, we perform in the next section a statistical analysis on a larger sample of objects.

3 STATISTICAL COMPARISON

In order to obtain more robust results, we merged our observations with other ones. We used the Leroy (1993a) catalogue which is an extensive polarization survey of precise measurements for 1000 stars closer than 50 pc. We note that his selection of stars was based on pre-*Hipparcos* distances. In addition to his own measurements, Leroy (1993a) compiled measurements from the literature that met his criteria. Gáspár et al. (2013), based on *Spitzer* MIPS and *Herschel* PACS data, were able to reliably determine the presence of FIR excess for more than 550 nearby stars. By combining these two lists with our observations and keeping the measurement with the best S/N ratio for each object, we have the polarization and the occurrence of FIR excess for 223 stars. We include also HR 8799 although it is not in the DEBRIS sample since its distance is compatible, < 46 pc, the limit for A-type stars. The results for 18 stars with detected polarization ($P \geq 3\sigma_P$) are presented in Table 1; those for the other stars are in Table A1 in Appendix.

Column 1 of Table 1 shows the star identification given by the DEBRIS and SONS surveys (Phillips et al. 2010, 2012), the first letter represents its spectral class and the number is a zero-padded

running number increasing with distance in each subsample. These identifiers are referred to by the acronym UNS, standing for Unbiased Nearby Stars, as in the original SUNS survey names. Column 2 gives the name of the primary star; the choice of name is generally in the order of preference: HD, HIP, GJ, LHS, NLTT, TYC, PPM, CCDM, other catalogue name and 2MASS, following Phillips et al. (2012). The other columns in Table 1 give the measured polarization and its uncertainty, the equatorial polarization angle of the polarization vector and its uncertainty. When the uncertainty of the measured polarization angle (given by eqn 1) is larger than the standard deviation of a completely random sample, $\pi/\sqrt{12} = 51.96^\circ$, the polarization angle is undefined. Finally, the last five columns in Table 1 represent respectively the distance (pc) and its uncertainty, the ratio of the polarization to the distance (P/d), the presence of a disk according to FIR excess (Gáspár et al. 2013), the source of the data and the observation dates for OMM data. When we measured the polarization of a given star many times (multiple dates appear in the table), the result given is the weighted mean of these measurements. Table A1 (Appendix A) follows the same format than Table 1 except that the two columns for the polarization angle contain "undefined values" for those stars with $P < 2\sigma_p$ for the OMM data or when the information was not available from Leroy (1993a).

The column with the authors is from the Leroy (1993a) paper with Simon (this paper) added where necessary. We also added Bhatt & Manoj (2000) who observed about 10 stars from the DEBRIS list. Observations from OMM were made at a wavelength of 766 nm. The other stars compiled by Leroy (1993a) were observed at various wavelengths between 400 nm and 600 nm depending on the observer. These differences in wavelength between observations was not relevant for Leroy (1993a) because he was studying the distribution of interstellar dust in the solar neighbourhood, so, all observations in the visible were suitable for his purpose. These differences in wavelength may be significant for interpretation in our case since polarization may vary with wavelength across the visible. In our numerical simulations we computed the polarization for the *I* band at 760 nm (see section 4.3).

3.1 Stars with $3\sigma_p$ polarization detection

Table 1 shows that 18 objects have a polarization level at or above $3\sigma_p$. Two of them, HD 7570 and HD 165908, have a detected FIR excess.

HD 165908, also known as 99 Herculis, is a binary system with F- and K-type stars at 16.5 AU from each other and with an imaged debris disk at 120 AU from the barycentre (Kennedy et al. 2012). Their preferred disk model is a ring of polar orbits that move in a plane perpendicular to the pericentre direction. The polarization angle is $158.9^\circ \pm 9.6^\circ$, as computed directly from the Pirola (1977) data. This means that the observed polarization is almost aligned with the pericentre position angle, at 163° , which is more or less the expected orientation of the polarization vector, although it should vary slowly in time with the orbit of the binary with a period of 56.3 yr (see e.g., Brown et al. (1978), Manset (2005)). Pirola (1977) did not mention the size of the aperture he used for his polarization observations. A diameter of 16 arcsec includes most of the disk, at the distance of HD 165908.

HD 7570 or ν Phenicis is a solar type star (F9 VFe) at 15 pc with confirmed IR excess (Gáspár et al. 2013; Cotten & Song 2016), but no disk has been imaged yet in this system. Beichman et al. (2006a) reported a *Spitzer* IRS 30–34 μm excess, extending out to 70 μm . They estimated $L_{\text{dust}}/L_\star = 4.3 \times 10^{-5}$ and modelled

this excess with a single-ring disk between 11–12 AU with 10 μm dust grains at about 100 K. The disk mass is $1.3 \times 10^{-6} M_\oplus$ assuming silicate grains with a density of 3.3 g cm^{-3} . Extrapolating the grain size distribution with a power of -3.5 out to 10-km diameter yields a mass of $0.042 M_\oplus$. A submm detection of the system would help constrain the dust size and distribution and hence the total mass. This star has a strong polarization detection, with $P = 0.075$ per cent ($P/\sigma_p = 12.5$) at a polarization angle of $47.7^\circ \pm 2.3^\circ$ (Korhonen & Reiz 1986). Given the level of polarization and assuming single scattering in an optically thin disk, the disk should have a significant inclination and a projected major axis oriented near a position angle of 138° .

There are 15 other stars with $3\sigma_p$ polarization detection but with no known IR excess. Such relatively low levels of polarization, $< P > = 0.023$ per cent, can arise from various situations. Seven systems are known to be spectroscopic binary or multiple star systems which breaks the axisymmetry of the system, resulting in a non-null polarization. Also, it might be a property of some variable stars since five of them are photometric variables. Finally, it is also possible that their disks are too faint to be detected in the FIR. Here is an example of a photometric and polarimetric variable. HD 137909 (β CrB) is a well-known α^2 CVn magnetic variable star with a spectral type of A8 V SrCrEu (Phillips et al. 2010; Gray et al. 2003). The broad-brand continuum linear polarization traces variations of the magnetic field component perpendicular to the line of sight as the star rotates (Leroy 1993a) with an amplitude of order $\sim 10^{-3}$. Phillips et al. (2010) had two entries for CCDM 15278+2906A and CCDM 15278+2906B as A065 in their Table 7, and also their Table in the Vizier catalogue. Both of them correspond to HD 137909 (= β CrB). Its polarization was detected by Leroy but not by Simon. This led us to two different entries for this star, the detection by Leroy in Table 1 and the non detection by Simon in Table A1. This has no significant effect on our statistics below.

Last, HD 115404 is a $3\sigma_p$ OMM detection, but there is no information about a possible FIR excess. It is a binary system which might explain the polarization detection. It consists of a K1 V star and a M1 dwarf and it has no known disk. As mentioned above, it is one detection in a sample of slightly more than one hundred stars (the OMM sample discussed in section 2.2 above), just the single detection expected statistically for such a sample. The polarization of this star should be confirmed by new observations.

3.2 Analysis

We divide our sample of 223 stars into 4 groups to compare their statistical properties. The A group contains objects with confirmed FIR excess as shown by Y in Tables 1 and A1. The group B contains group A stars plus those suspected to have a FIR excess or for which no confirmation is available yet (Y + ? in Tables 1 and A1). Group C contains only those suspected to have a FIR excess or for which no confirmation is available yet (? in Tables 1 and A1). And the last group, D, contains stars known for not having a FIR excess (N in Tables 1 and A1). The cumulative distribution function for the polarization of each group and of the total sample is given in Figure 2.

For each group we computed different parameters presented in Table 2. The columns in the table show: group identification and in parentheses the FIR excess status, the number of stars in each group, the number of stars with a detected polarization, i.e. with $P \geq 3\sigma_p$, the detection rate and its uncertainty based on the two previous columns, the (unweighted) average polarization $\langle P \rangle$,

Table 1. All stars observed at OMM and from the Leroy compilation with a polarization $P \geq 3\sigma_P$.

UNS ID	HD	P (10^{-5})	σ_P (10^{-5})	$\theta(^{\circ})$	$\sigma_{\theta} (^{\circ})$	P/σ_P	Distance (pc)	P/d (10^{-5}pc^{-1})	FIR ^a excess	Observers ^b	Date ^c
K046	115404	152	43	8.4	7.4	3.5	11.095 ± 0.090	13.7 ± 3.9	?	SI	22 Jan
G013	101501	24	8	ind. ^d	ind.	3.0	9.602 ± 0.024	2.5 ± 0.8	N	BE	
G052	142373	15	5	ind.	ind.	3.0	15.894 ± 0.053	0.9 ± 0.3	N	PI WA LE SE	
F002	170153	38	12	ind.	ind.	3.2	8.032 ± 0.033	4.7 ± 1.5	N	TI WA	
F009	102870	26	8	ind.	ind.	3.3	10.928 ± 0.026	2.4 ± 0.7	N	TI SE BE MA	
F013	210027	10	3	ind.	ind.	3.3	11.719 ± 0.086	0.9 ± 0.3	N	PI WA SE BE	
F016	147584	26	7	ind.	ind.	3.7	12.113 ± 0.076	2.2 ± 0.6	N	TI MA	
F021	222368	12	4	ind.	ind.	3.0	13.716 ± 0.028	0.9 ± 0.3	N	SC PI MA BE	
F029	176051	24	6	ind.	ind.	4.0	14.881 ± 0.081	1.6 ± 0.4	N	WA	
F032	7570	75	6	47.7	2.3	12.5	15.115 ± 0.055	5.0 ± 0.4	Y	KO TI SC	
F037	165908	15	5	159.9	9.6	3.0	15.660 ± 0.083	1.0 ± 0.3	Y	PI WA SE	
F040	76943	14	3	ind.	ind.	4.7	16.061 ± 0.172	0.9 ± 0.2	N	PI TI BE	
F075	119756	90	30	ind.	ind.	3.0	19.407 ± 0.072	4.6 ± 1.5	N	MA	
A017	118098	29	8	ind.	ind.	3.6	22.724 ± 0.098	1.3 ± 0.4	N	TI BE MA	
A026	106591	15	5	ind.	ind.	3.0	24.688 ± 0.085	0.6 ± 0.2	N	PI TI BE	
A065 ^e	137909	80	10	ind.	ind.	8.0	34.281 ± 0.892	2.3 ± 0.3	N	LE	
A106	210049	20	4	ind.	ind.	5.0	41.592 ± 1.674	0.5 ± 0.1	N	SC	
A130	16555	22	6	ind.	ind.	3.7	45.538 ± 2.276	0.5 ± 0.1	N	SC	

^a Detection of FIR excess: yes (Y), no (N), no information or uncertain (?).

^b Abbreviations for the observers are, respectively, ‘SI’ for this paper (Simon), ‘AP’ for Appenzeller (1968), ‘BE’ for Behr (1959), ‘BM’ for Bhatt & Manoj (2000), ‘HU’ for Huovelin et al. (1985, 1988); Huovelin & Pirola (1990), ‘KO’ for Korhonen & Reiz (1986), ‘KR’ for Krautter (1980), ‘LE’ for Leroy (1993a), ‘MA’ for Mathewson & Ford (1970), ‘PI’ for Pirola (1977), ‘SC’ for Schröder (1976), ‘SE’ for Serkowski (1970), ‘TI’ for Tinbergen (1982) and ‘WA’ for Walborn (1968).

^c Observations from OMM were obtained during the winter 2009–2010.

^d When the uncertainty on the polarization angle is larger than $\approx 52^{\circ}$, its orientation is indefinite (see text). Also it is customary not to give the polarization angle when the polarization is considered to be too small to yield a reliable polarization angle.

^e As explained in section 3.1, there are two entries for this star, here and in Table A1.

Table 2. Summary of the polarization statistics for each group of stars. The description of the samples and the meaning of each column are given in the text. The units for the polarization and uncertainties are 10^{-5} .

Sample	N	$N_{P>3\sigma}$	det. rate ^a	$\langle P \rangle^b$	$\langle \sigma_P \rangle^c$	ζ_P^d	$\zeta_{\sigma_P}^e$
A (Y)	28	2	7^{+8}_{-2} %	23	23	14	11
B (Y+?)	88	3	3 ± 2 %	33	38	28	19
C (?)	60	1	2 ± 2 %	38	42	34	18
D (N)	135	15	11 ± 3 %	25	26	17	16
All	223	18	8 ± 2 %	28	32	21	18

^a Given the small numbers involved, the binomial distribution is appropriate.

We computed 1σ uncertainties following Burgasser et al. (2003).

^b Mean polarization of the groups.

^c Mean uncertainties of the groups.

^d Square root of the variance of the polarization of the groups.

^e Square root of the variance of the uncertainties of the groups.

the (unweighed) average uncertainty of the measurements $\langle \sigma_P \rangle$, the standard deviation of the polarization measurements ζ_P , and the standard deviation of the uncertainties ζ_{σ_P} . The first point we can observe is even if the average polarization differs between the different groups, in particular A, C and D, these differences are not significant because they are smaller than $\langle \sigma_P \rangle$ and ζ_P . Checking the mean of the measurement uncertainty, $\langle \sigma_P \rangle$, and the statistical uncertainty on these, ζ_{σ_P} , we can see the same variation pattern. Finally no significant differences have been found between the different groups except for the measurement precision. We note that the sample about which we have less information (C) is also the less precise one.

Table 3. Results of the Kolmogorov–Smirnov (KS) tests between different debris-disk groups with respect to polarization detection.

	A vs. C	A vs. D	C vs. D
KS coefficient	0.310	0.159	0.260
p-value	0.042	0.581	0.005

To pursue the analysis further, we performed a Kolmogorov–Smirnov (KS) test for different combinations of the stellar groups. We tested the “null hypothesis”, H_0 : “The two groups of stars tested through polarization data come from the same population of stars,”

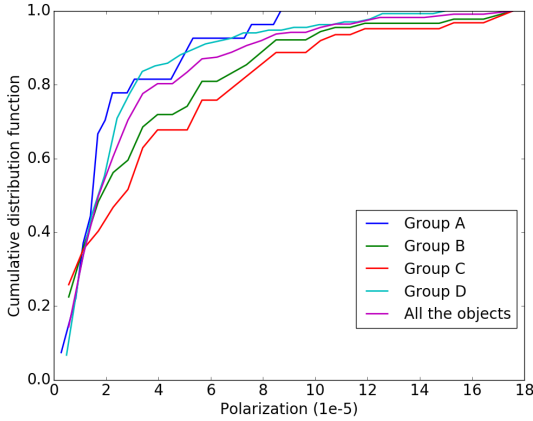


Figure 2. Comparison of the polarization cumulative distribution function (CDF) for each group of stars defined by their presence of FIR excess. The fractional number of stars with observed polarization smaller than a given value is given as a function of the polarization. Groups A, B, C and D as defined in section 3.2 are represented by the colours dark blue, green, red and light blue respectively. The purple line corresponds to the distribution for the entire sample.

i.e. the two groups of stars tested have the same polarization Cumulative Distribution Function (CDF). The KS statistics, D_{KS} , obtained with the KS test represents the maximum distance between the CDF of two groups being compared. We set a confidence level α and for each statistical test compute a critical value C_α ¹ depending on α and the number of elements in the list. Then, we can reject H_0 with a confidence level of α if D_{KS} is greater than C_α . In Table 3, KS results are generally low. We have to choose a low level of confidence ($\alpha = 0.1$), to reject H_0 for A versus C (where $C_\alpha \approx 0.28$) and C versus D (where $C_\alpha \approx 0.19$). So, we can reject H_0 for A versus C and C versus D but not for A versus D. Since we used a low level of confidence, checking H_0 with another parameter would help to confirm our conclusions. The KS test also computes the p-value which represents the believability that H_0 can be rejected². With those results, we notice that the null hypothesis can be rejected for A vs. C and for C vs. D. In conclusion, the probability that the samples have consistent CDF's statistics is very low and we can confidently reject H_0 for A versus C and C versus D tests. For the A versus D test, we cannot reject the null hypothesis, i.e., they may come from the same population of stars.

To summarize, we can conclude that sample C is different from samples A and D but that sample A may be consistent with D. So, the conclusion of the KS test is unexpected: the two samples we would legitimately assume as different could possibly match; and the samples that should match are, in fact, different. This is consistent with Figure 2 where group C presents the largest differences with the other groups.

Bhatt & Manoj (2000) made a similar comparison for 61 stars and they found a larger polarization for Vega-like stars (i.e., stars with debris disks) than for normal field stars. They observed 27 stars with known IR excess and selected measurements for 34 additional stars with IR excess from the Heiles (2000) catalogue. Uncertainties on measurements in the Heiles catalogue are ≈ 0.1

¹ Tables can easily be found in literature.

² If $p \leq \alpha$, H_0 may be rejected; but if $p > \alpha$ we cannot conclude about the validity of H_0

per cent. The distances for these stars are significantly greater than those used here; only about 10 of them are in the DEBRIS list.

3.3 Conclusion

When we compare the groups with and without FIR excess (A vs. D), we find that there is no statistically significant difference for their 3σ -polarization detection rate, nor for the shape of their cumulative polarization distribution functions. This is also confirmed by the KS test. The group that differs the most from the other ones is group C, the objects without FIR excess confirmation.

These results seem to indicate that there is no correlation between the presence of a disk and the observed level of polarization. But, we should not forget that the great majority of our polarizations are below the 3σ level and that the detection rate obtained is smaller than the fraction of stars with debris disks, around 20 per cent. This last statement, a polarization rate smaller than the fraction of stars with debris disks, would be expected since polarization also depends on the orientation of the disks with respect to the observer. However, it is also likely that some debris disks are not detected because their IR emission is too low but their polarization can nevertheless be detected. If this is the case, it should depend on the sensitivity of the IR detectors relative to that of the polarimeters used. This goes against our equation 9 (see section 5.2), but is not impossible. So, we cannot conclude firmly about the link between disks and polarization based on observations only.

In order to complete our investigation about this link we now turn to analytical models and simulations.

4 MODELS

A conclusion of the previous sections is that few systems have a linear polarization above the typical threshold of $P \sim 10^{-4}$ integrated through an aperture. In particular, we see in Table 1 that the polarization of detected stars ranges from about 1 to a few $\times 10^{-4}$. In the following, we will consider $P = 10^{-4}$ as a polarization limit and investigate the constraints it imposes and its implications for the mass of circumstellar dust in these systems. This polarization threshold can be considered as a practical limit between classical and high-precision polarimeters and will be used as a reference here.

4.1 Analytic approach

We consider a toy model in which a cloud of identical dust grains is placed at a unique distance and unique azimuth from the star. Such a configuration mimics the case of an isolated blob of dust, but we acknowledge that this most likely does not correspond to any realistic situation but a scenario which maximises the polarization for a given dust mass. The scattering angle of 90° maximizes approximately the polarization signal, and yields an estimate of the minimum dust mass necessary to reach a $P = 10^{-4}$ polarization level. Assuming unpolarized incident light, the degree of linear polarization P , measured by the observer with aperture polarimetry, is given by

$$P = \frac{P_{\text{dust}} I_c}{I_\star + I_c + I_{\text{th}}}, \quad (2)$$

where P_{dust} is the degree of linear polarization for scattering by one grain, I_c the intensity of stellar light scattered by the dust cloud, I_\star the stellar intensity and I_{th} the thermal grain emission at the considered wavelength. The degree of linear polarization of one grain

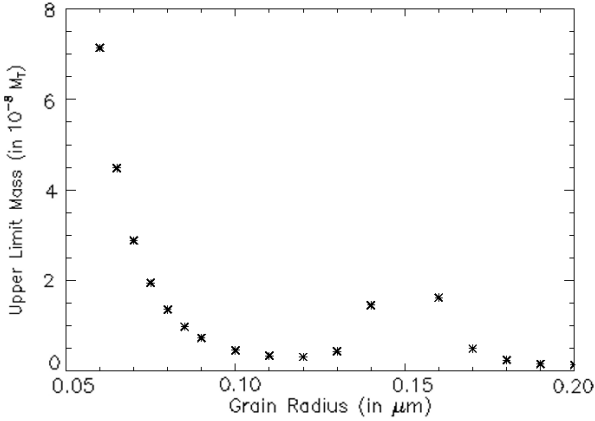


Figure 3. Mass of the disk determined as a function of the grain radius, for an assumed observed polarization of 0.1 per cent. The mass is given in terrestrial mass, ($M_{\text{T}} = M_{\oplus}$). Other assumptions are given in the text. There is no symbol for a radius of $0.15 \mu\text{m}$ due to the very low polarization induced by grains of this size. This leads to a very high disk mass, larger than the scale of this figure.

(P_{dust}) and the scattered intensity of the cloud (I_{c}) are given by (see e.g., Bohren & Huffman (1998)):

$$P_{\text{dust}} = \frac{i_1 - i_2}{i_1 + i_2}, \quad I_{\text{c}} = NI_{\star} \frac{i_1 + i_2}{2k^2 r^2} = NI_{\star} y, \quad (3)$$

where i_1 and i_2 denote the scattered-light fractional intensities polarized perpendicular and parallel to the scattering plane, respectively, r is the distance to the star, k the wavenumber and N the number of grains. This number of grains is linked to the dust mass M of the disk by $M = \rho V N$ with ρ the grain density (we used the value of 3 g cm^{-3} for astronomical silicates) and V the volume of one grain.

Combining equations 2 and 3, and anticipating that $I_{\text{c}} + I_{\text{th}} \ll I_{\star}$, we obtain the dust cloud mass

$$M \simeq \frac{P \rho V 2 k^2 r^2}{i_1 - i_2}. \quad (4)$$

Combining equations (2) and (3), we then have

$$P = P_{\text{dust}} N \left[\frac{y}{1 + Ny + I_{\text{th}}/I_{\star}} \right]. \quad (5)$$

The polarization induced by debris disks will decrease approximately as the square of their distance from the star, as can be seen in equation (5) and remembering that $y \propto r^{-2}$ (see equation 3). Note that the last two terms in the denominator are negligible since $I_{\text{c}} + I_{\text{th}} \ll I_{\star}$ in the visible and NIR (see e.g., Schneider et al. (2014)). Therefore, for a given mass (or number of dust grains, N), this survey is more sensitive to hot debris disks such as the zodiacal cloud in our solar system. In this simple model, we assume arbitrarily that all grains are at 1 au. This is a representative distance such that grains are warm enough and such that polarimetric measurements are sensitive.

Fixsen & Dwek (2002) estimated that grain radii in the zodiacal cloud range from $0.01 \mu\text{m}$ to 1 cm, decreasing exponentially. For our simple model, we use a grain radius of $0.1 \mu\text{m}$. We modelled the grains with astronomical silicates and took the complex refractive index from Draine (1985) at $0.870 \mu\text{m}$: $m = n + ik$ with $n = 1.71$ and $k = 0.0297$. Using Mie scattering theory, we computed numerically the Van de Hulst intensities, i_1 and i_2 , for a given

grain radius and scattering angle. Figure 3 shows how other grain sizes will change the total mass.

With all these assumptions, we find a disk mass of $0.1 \mu\text{m}$ -sized grains of $4.5 \times 10^{-10} M_{\oplus}$ for $P = 10^{-4}$. Note that Figure 3 is scaled for $P = 10^{-3}$. As mentioned above, this model finds the minimum mass of grains with a given radius that can produce a polarization $P = 10^{-4}$. This is the case because we use a single position at 1 au for all the scattering dust grains and also a single scattering angle of 90° which is near the maximum of the scattering phase function. If conditions are less favourable, a larger mass will be necessary to reach the same polarization. Since the zodiacal cloud mass has been evaluated at between $0.33 - 1.8 \times 10^{-9} M_{\oplus}$ by Fixsen & Dwek (2002), and at $\sim 8 \times 10^{-9} M_{\oplus}$ by Nesvorný et al. (2010) based on dynamical models and IRAS data, we indeed are at the limit of sensitivity of the instrument, if extrasolar hot debris disks resemble the zodiacal cloud.

Single scattering by Mie particles in optically thin envelopes around a star has been considered in the past and can be applied in the context of our paper. Bastien (1987) studied analytically the properties of different geometries. For an azimuthally symmetric but otherwise arbitrary density distribution, the polarization is proportional to $\sin^2 i$ as long as grains are relatively small compared to the wavelength, i.e., $x = ka = 2\pi a/\lambda < 2.0$, where a is the grain radius and i is the inclination of the disk. For a plane disk, the polarization is given by (Bastien 1987):

$$P \propto \frac{15}{4} [N' \sin^2 i] \bar{F}_{22}, \quad (6)$$

where N' is an integral over the radial density distribution in the disk, and \bar{F}_{22} is real and depends on the scattering phase function (Simmons 1982). \bar{F}_{22} also determines the wavelength dependence of the polarization. The polarization angle is usually perpendicular to the disk, except for a possible change by $\pi/2$ when \bar{F}_{22} changes sign. In all cases, we see that there is a strong, sine square, dependence on the inclination. This dependence on inclination is responsible for the non detection of polarization for a large fraction of stars which have been detected by IR surveys (see section 3.2), simply because they do not show a favourable configuration towards Earth to generate a significant polarization.

4.2 Simulations of dust belts

Complementary to our analytical toy model, we performed extensive simulations with MCFOST (Pinte et al. 2006), a Monte Carlo Radiative Transfer (MCRT) code. These results enable us to investigate the influence of many parameters on the polarization of unresolved objects. As earlier, we assume a detection threshold of 10^{-4} for linear polarization.

We then computed 2-D maps for all Stokes parameters at $\lambda = 0.76 \mu\text{m}$ (which is approximately the central wavelength of the bandpass used by Beauty and the Beast), with the size of the map corresponding to the extent of the disk itself.

The most important parameter to investigate is the distance between the inner edge of the disk and its star. As explained earlier, closer the disk is located, higher the polarization will be. But the large field of view of aperture polarimeters cannot be used to constrain belt locations. As a consequence, the spectral type of the star is the parameter that constrains the location of the disk: smaller and colder the star is, closer the disk can be. As a consequence, we tested 4 spectral types as shown in Table 4.

In order to compare disks, we use the temperature as a key

Table 4. Stellar data used in the calculations. The assumed synthetic spectral distribution of each star comes from NextGen simulations (Hauschildt et al. 1999). Data in the table are from Allen (1973).

Spectral Type	R/R_{\odot}	M/M_{\odot}	T (K)	$\log g$	L/L_{\odot}
A0	2.40	2.90	9790	4.13	47
F5	1.30	1.40	6650	4.36	3
K0	0.85	0.79	5150	4.48	0.46
M2	0.50	0.40	3520	4.64	0.032

Table 5. Values of inner (r_{in}) and outer (r_{out}) radii for the belts around four representative stars computed from temperatures given in the text.

		Hot	Warm	Cold
A0	r_{in} [AU]	0.236	5.9	212
	r_{out} [AU]	5.9	212	332
F5	r_{in} [AU]	0.059	1.49	53.7
	r_{out} [AU]	1.49	53.7	83.8
K0	r_{in} [AU]	0.023	0.584	21.0
	r_{out} [AU]	0.584	21.0	32.8
M2	r_{in} [AU]	0.020	0.502	18.1
	r_{out} [AU]	0.502	18.1	28.2

parameter to set the inner and outer radii of each disk, mimicking roughly those from the solar system³.

For hot disks the inner edge, r_{inhot} , is set at the dust sublimation radius crudely estimated assuming blackbody emission/absorption dust properties and thermal equilibrium:

$$R_{\text{sub}} = \sqrt{\frac{L_{\star}}{\pi\sigma_s}} \frac{1}{4T_{\text{sub}}^2}, \quad (7)$$

where L_{\star} is the stellar luminosity, σ_s , the Stefan-Boltzmann constant, and T_{sub} the sublimation temperature assumed equal to 1500 K, representative of typical silicate grains. Other inner radii are set to match typical temperatures: 300 K for r_{outhot} and r_{inwarm} , 50 K for r_{outwarm} and r_{incold} and finally 40 K for r_{outcold} . The radii computed for each representative star are shown in Table 5. A typical mass for each one of these disks is given in Table 6. These masses come from the literature (Absil et al. 2006; Beichman et al. 2006a; Najita & Williams 2005; di Folco et al. 2007; Rhee et al. 2007; Wyatt et al. 2003; Wyatt & Dent 2002; Lebreton et al. 2013) and were obtained from observations and/or disk modelling. We also used more recent information, presented in the second part of Table 6 for various spectral types from B8 to M2, but only 2 M-type stars are included (cold belts). Values for hot belts come from a reanalysis with detailed models by Kirchsclager et al. (2017) of published interferometric data. Warm belt values come from a compilation of *Spitzer* (63) and *WISE* (11) detected disk measurements by Gáspár et al. (2016). We note that the average of the *WISE* masses is about 50 times smaller than the average of only the *Spitzer* data. Finally, data for cold belts come from the SONS survey (Holland et al. 2017).

We studied the influence of the power-law grain size distributions. We assumed spherical, amorphous silicate grains [see Draine (1985) for the optical constants], with sizes going from $a_{\text{min}} \in$

³ Exozodiacal, asteroidal and Kuiper belts are also called hot, warm and cold belts.

Table 6. Typical mass in M_{\oplus} unit for each disk.

	Hot belts	Warm belts	Cold belts
A0	2×10^{-6}	3×10^{-4}	1×10^{-2}
F5	3×10^{-7}	2×10^{-4}	4×10^{-3}
K0	3×10^{-8}	6×10^{-5}	3×10^{-3}
M2	4×10^{-9}	2×10^{-5}	1×10^{-3}
$\langle M \rangle^a$	2×10^{-9}	8×10^{-5}	9×10^{-2}
Range	$(0.2 - 4) \times 10^{-9}$	$1 \times 10^{-7} - 1 \times 10^{-3}$	$2 \times 10^{-4} - 0.4$
N	9	74 (63 + 11)	46

^a This section of the table presents the average mass, the range of masses covered by the sample and the number of stars in the sample, N . The sample includes stars of spectral types A, F, G and K, plus a few B8 and M-types. See text for additional information.

$\{10^{-1}, 1, 10\} \mu\text{m}$ to a_{max} fixed to 1 mm. Tiny grains dominate the scattering process because of their higher relative cross sections. Selecting a different a_{min} is equivalent to adding or removing tiny dust grains: it leads to an increase or a decrease of the scattering efficiency for a given total dust mass.

The same effect is observed as we varied the index of the exponent in the power law of the grain size distribution: $\kappa = 3, 3.5$ and 4. Finally, the effects of some geometrical factors were studied such as the surface density profile also defined as a power law, with index $\alpha = -3.5, -2$ and -0.5 , and the thickness of the disk, an important geometrical factor, given by a gaussian vertical profile with a scale height defined as $H/r = 0.05$.

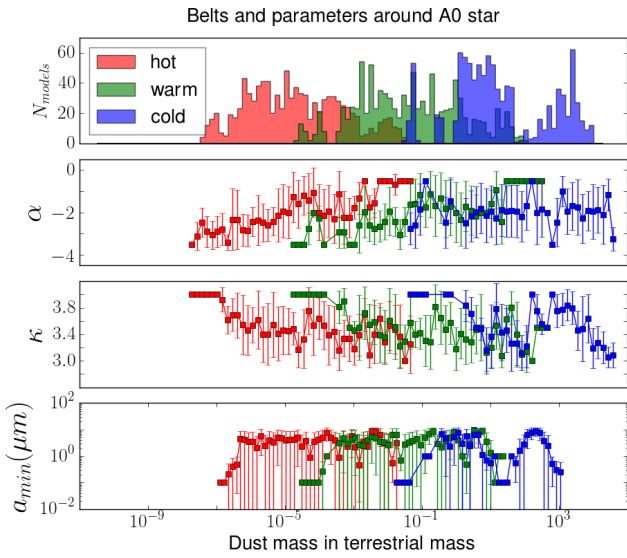
Finally we studied the influence of disk asymmetries. Debris disks are present in evolved planetary systems, and *Kepler*'s results have shown that there is a significant fraction of stars with planets. If planets are sufficiently massive, they will affect significantly the disk geometry as shown by Faramaz et al. (2014) for example. One of the most important effects is to break axial symmetry, creating elliptical orbits or ellipses instead of circular rings. With this geometry, one section of the ellipse will be closer to the star than the other ones. When the belt is a circular ring, every location along the ring produces the same linear polarization fraction as seen pole-on, and the polarization from each location is cancelled by another location at 90° from it. The result is a net zero polarization. But this is no longer the case when axial symmetry is broken as polarization vectors will not cancel out. Our purpose here is to obtain a rough quantitative estimate of this effect on polarization and therefore on our mass detection threshold. The most important effect of this symmetry breaking is the differential amount of energy coming from the star on the disk. To mimic this effect we just move the star from the centre of the ring that we still model as a circle. Eccentricity is typically around 0.3 to 0.4 such as for example Fomalhaut (Boley et al. 2012). To cover this range of eccentricities we move the star from the centre of the disk by respectively 0 per cent, 30 per cent and 60 per cent of the inner radius of the belt.

Combining all those elements, 4 spectral types, 3 disk types, 3 minimum grain sizes, 3 power-law exponents for the grain size distributions and 3 exponents for the surface density distributions and 3 stellar offsets, yields a computational grid of 972 disk models. The FITS file produced by each model has 12 relevant images for 3 disk inclinations and 4 disk azimuths (described below in 4.3), leading to 11 664 elements to analyse. In summary, for each combination of spectral type and type of disk, there are 4 parameters

Table 7. Values of the parameters used in the computational grid.

Parameter name ^a	minimum value	mid value	maximum value
a_{\min} (μm)	0.1	1	10
κ	3	3.5	4
α	-3.5	-2	-0.5
Star's position	0	$0.3r_{\text{in}}$	$0.6r_{\text{in}}$

^a The first two parameters specify the grain size distribution: minimum grain size and power-law index. α is the surface density exponent of the disk and the stellar position is used for simulating eccentric disks (see Fig. 5).



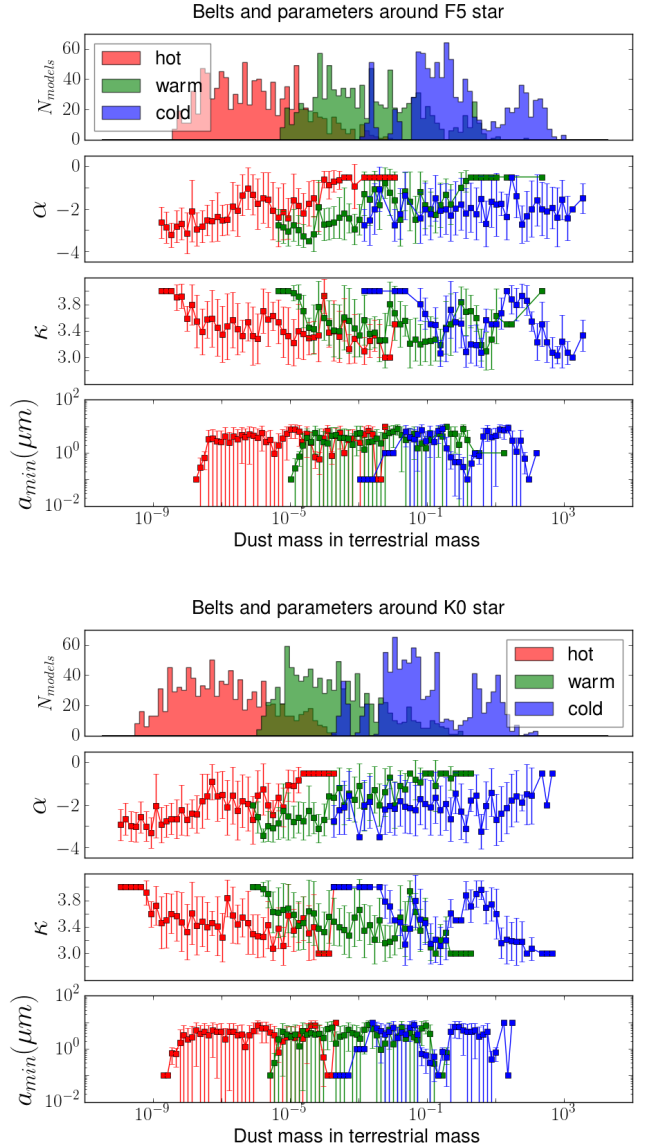
considered (see Table 7). And each one of these models includes different inclinations and azimuths.

For each model we compute the dust mass consistent with our detection threshold, $P = 10^{-4}$. For the computations, we adopt a fiducial distance of 10 pc from the observer. We note that the degree of polarization does not depend on this assumption: the polarized and total intensities and their ratio all scale as the square of the distance. We do not consider interstellar polarization in our calculations, but will discuss its effects on observed debris disks later in section 5.

4.3 Results

For each star and set of parameters MCFOST computes a synthetic cube of images of the Stokes parameters I , Q , U and V at $\lambda = 0.76 \mu\text{m}$. These image cubes are computed for four different azimuthal angles ($\phi = 0^\circ, 30^\circ, 60^\circ$ and 90°) and three inclination angles ($i = 0^\circ, 30^\circ$ and 90°). Finally, a simple python algorithm computes the total integrated linear polarization of the synthetic pictures.

We assume optically thin disks, i. e. the total polarization is proportional to the disk mass, according to equation (5) above. Therefore we can scale the mass to make it correspond to the degree of linear polarization $P = \sqrt{Q^2 + U^2}/I = 10^{-4}$, our assumed detection threshold. The scattered radiation is small compared to the stellar radiation. This is also the case for the dust thermal emission at $0.76 \mu\text{m}$.



These mass values are used to derive mass distributions for all of our disk models. These histograms are displayed in the top panel for each spectral type in Figure 4. There are 84 mass bins, or about 7.3 bins per mass decade. For each mass bin, we computed the mean value and a standard deviation for three relevant parameters in order to identify trends, if present. Keeping in mind that the size and definition of the computational grid is limited, we then analysed those trends to estimate which parameters have more influence on the polarization and the disk detectability. The mean values and their standard deviations for the parameters are displayed in Figure 4, below their respective histograms.

4.3.1 Mass study

The histograms in Figure 4 show the presence of peaks for each type of belt. These peaks are the result of the grid discretization of the various parameters we used. They do not reflect an expected mass distribution for these belts. The values of the parameters selected are model dependent and represent best guesses for the range of values they might take. The choices made are based on models used to represent spectral energy distributions (SEDs) obtained

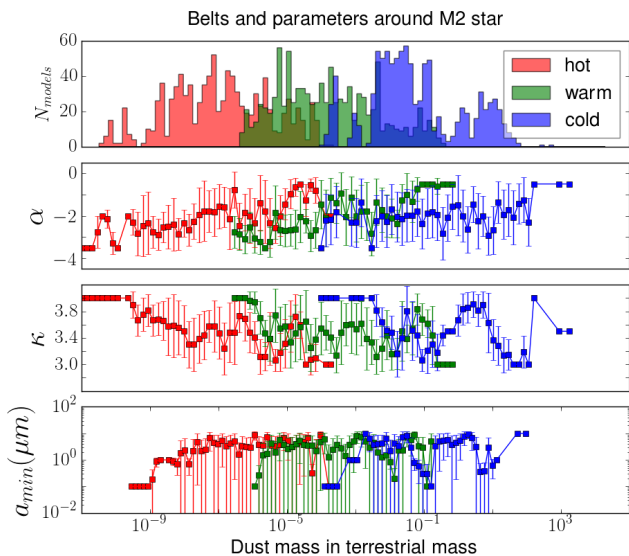


Figure 4. Histograms representing the number of simulations sorted by the mass of the minimum detectable mass of their disks. All 972 disk models are used, including the three stellar positions for simulating eccentricity. Underneath we plot the mean values in each mass bin for the surface density exponent α , the grain-size distribution power-law index κ , and the minimum size of the grains, a_{min} , for the 4 spectral types and 3 belts considered (see Table 7). The error bars correspond to 1σ and vary according to the number of simulations in each mass bin.

Table 8. Mass ranges in M_{\oplus} unit covered by our simulations for each belt and the four spectral types. The ranges are defined by their 10, 50 and 90 percentiles from the models. The masses correspond to the mass needed to produce a polarization of 10^{-4} .

		Hot	Warm	Cold
A0	10%	1.0×10^{-6}	6.6×10^{-4}	1.6×10^{-1}
	50%	2.7×10^{-5}	2.5×10^{-2}	3.1
	90%	1.6×10^{-3}	2.1	4.1×10^2
F5	10%	9.2×10^{-8}	4.6×10^{-5}	1.0×10^{-2}
	50%	1.9×10^{-6}	1.3×10^{-3}	1.9×10^{-1}
	90%	1.0×10^{-4}	1.1×10^{-1}	2.3×10
K0	10%	1.2×10^{-8}	1.0×10^{-5}	1.5×10^{-3}
	50%	2.7×10^{-7}	1.7×10^{-4}	2.8×10^{-2}
	90%	1.7×10^{-5}	1.0×10^{-2}	3.0
M2	10%	9.6×10^{-9}	5.4×10^{-6}	1.1×10^{-3}
	50%	3.1×10^{-7}	1.6×10^{-4}	2.0×10^{-2}
	90%	2.2×10^{-5}	1.4×10^{-2}	2.5

from NIR to submm data currently available. To make progress, we are going to assume that the histograms give us a range of masses to be expected for the three types of belts. To make this simpler, we present in Table 8 the mass range covered by each belt according to their 10, 50 and 90 percentiles as determined from our simulations.

With this assumption, we now perform comparisons between our model simulations and real measurements of belts in the literature to find out how feasible belt detection is with unresolved polarization. For hot belts around A0 stars, the literature typically obtains masses of $2 \times 10^{-9} M_{\oplus}$ (Absil et al. 2006, 2008; Defrère et al. 2011; Kirchschrager et al. 2017) for Vega, $2.0 \times 10^{-10} M_{\oplus}$ for

Fomalhaut (Lebreton et al. 2013; Kirchschrager et al. 2017), both of them much lower than the range of typical masses required to obtain a polarization of 10^{-4} (Table 8), starting at $1 \times 10^{-6} M_{\oplus}$. The G8 star τ Ceti has an exozodi disk first evaluated at $\sim 1 \times 10^{-9} M_{\oplus}$ by di Folco et al. (2007). Kirchschrager et al. (2017) estimated a minimum mass of $3 \times 10^{-11} M_{\oplus}$ and a maximum mass from $1.2 \times 10^{-9} M_{\oplus}$ (face-on) to $2.4 \times 10^{-9} M_{\oplus}$ (edge-on). τ Ceti can be compared to our F5 star. The median of the mass range corresponds to a hot disk of $2 \times 10^{-6} M_{\oplus}$ and the mass range goes down to almost $10^{-7} M_{\oplus}$. Kirchschrager et al. (2017) modelled 6 other stars, including ζ Cep with a maximum mass up to $5 \times 10^{-8} M_{\oplus}$ and 10 Tau with a maximum mass up to $5 \times 10^{-7} M_{\oplus}$. Only the F9 IV-V star 10 Tau could, if the best conditions prevail, hope to be detected within our polarization threshold. Note that these two extreme values for ζ Cep and 10 Tau were not taken into account in Table 6 as they are not typical values. As seen already with our toy model above (section 4.1), our own zodiacal cloud around our G2 star would not be detected according to our simulations if we observed it from a distance since it falls below the expected mass range. Since we assumed that those detections were the best case scenario, it implies that hot belts require a polarization precision better than 10^{-4} , our detection threshold.

Warm belts around solar-type stars have been studied more extensively by Lawler et al. (2009) who covered a spectral range from F1 to K3. They used *S pitzer* data and the models for their detected disks have dust masses from $\sim 4 \times 10^{-8} M_{\oplus}$ to $\sim 2 \times 10^{-4} M_{\oplus}$. These masses have been computed assuming $10 \mu\text{m}$ grains only with a density for silicates of 3.3 g cm^{-3} . Comparing with results from the mass histograms which have masses ranging upwards from 5×10^{-6} , 1×10^{-5} , and $5 \times 10^{-5} M_{\oplus}$ for M2, K0 and F5 stars respectively, according to the 10 percentiles listed in Table 8, we conclude that a few of the more massive warm dusty disks seen by *S pitzer* (HD 10647, HD 38858 and HD 45184) are slightly above our polarization detection threshold. The first of these stars also hosts a planet and a cold disk detected at $160 \mu\text{m}$ by *S pitzer* (Tanner et al. 2009). The A star Fomalhaut has a warm disk at about 2 AU with a mass between 2 and $3 \times 10^{-6} M_{\oplus}$ (Lebreton et al. 2013), a value about a few times lower than the lower bound of the mass range for disks in our simulations. The more recent study by Gáspár et al. (2016) includes more stars and better models and the mass values for the whole sample are presented in Table 6. This paper reports 24 stars with $M > 1 \times 10^{-5} M_{\oplus}$, 16 stars with $M > 5 \times 10^{-5} M_{\oplus}$, 7 stars with $M > 1 \times 10^{-4} M_{\oplus}$ and 2 stars with $M > 1 \times 10^{-3} M_{\oplus}$. The stars with $M > 10^{-4} M_{\oplus}$ are (with spectral types): HD 15745 (F0), HD 39060 ($=\beta$ Pic; A6 V), HD 80950 (A0 V), HD 106906 (F5 V, a member of the Lower Centaurus Crux association), HD 111520 (F5/6 V), HD 119718 (F5 V) and HD 145560 (F5 V). These 7 stars have spectral types A or F and they all have a mass higher than the 10 percentiles listed in Table 8.

For cold belts, lower bounds for detectable masses in polarimetry range from $1 \times 10^{-3} M_{\oplus}$ for M2 stars to about $0.2 M_{\oplus}$ for A0 stars (Figure 4 and Table 8). The SONS JCMT/SCUBA-2 survey reports 46 detections of cold belts in a sample of 100 candidate stars (Holland et al. 2017) with spectral types ranging from M2 to B8 and distances up to 96 pc (beyond the limit of our sample). Their dust masses computed from the submm fluxes range from $2 \times 10^{-4} M_{\oplus}$ (τ Ceti) to $0.37 M_{\oplus}$ (HD 98800) with an average mass of $0.09 M_{\oplus}$. The stars HD 181327 (Lebreton et al. 2012), Fomalhaut (Acke et al. 2012; Lebreton et al. 2013), HD 115617 and HD 207129 (Tanner et al. 2009) are included in the SONS detections. The stars HD 10647 and HD 38858 with detected warm disks mentioned above, were also detected by SONS. Therefore many

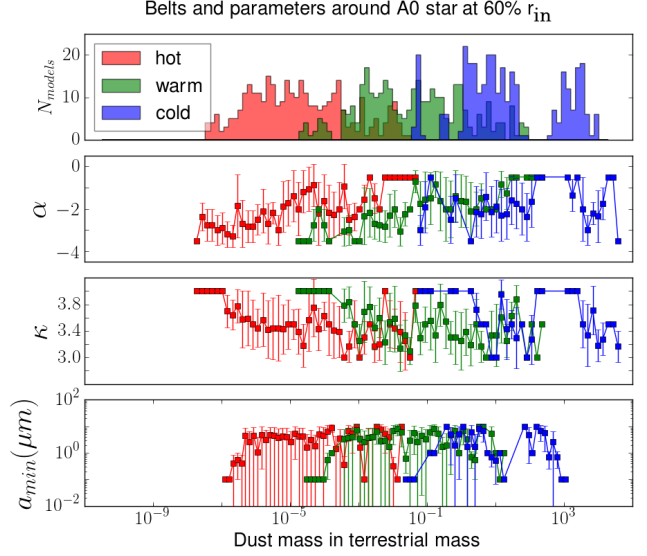
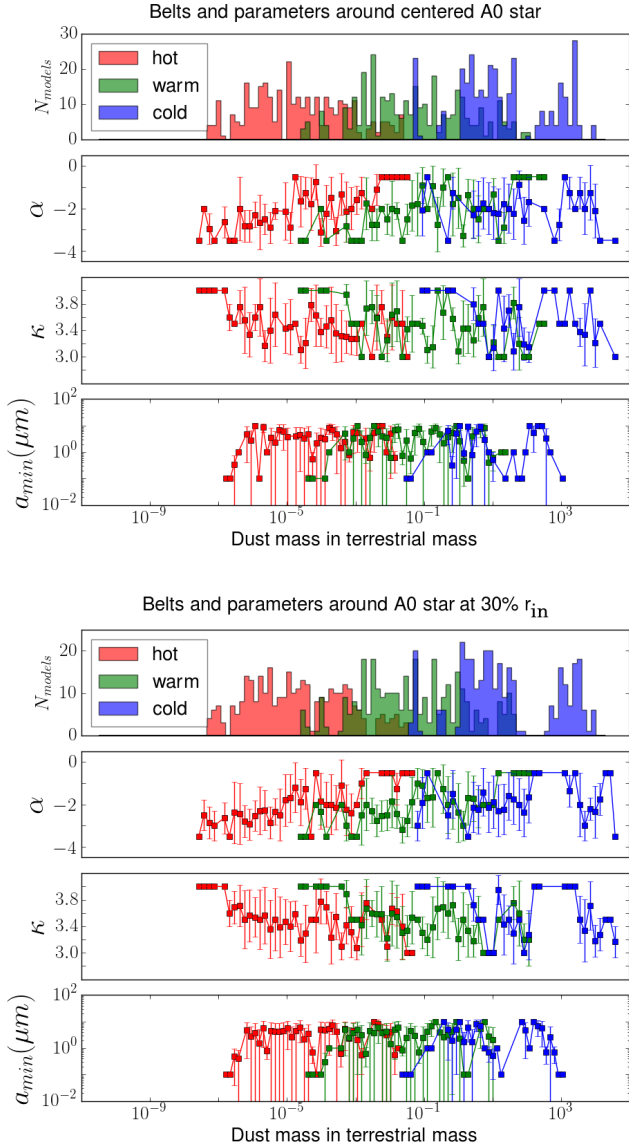


Figure 5. Histograms representing the number of simulations sorted by the mass of the minimum detectable mass of their disks. These histograms present results for only the A0 star and correspond to the top panel of Figure 4 split into 3 parts to compare the outcome for each stellar position, centered, at 30 and 60 per cent of r_{in} . Underneath we plot the mean values in each mass bin for the surface density exponent α , the grain-size distribution power-law index κ and the minimum size of the grains, a_{min} , for the 3 stellar positions and 3 belts considered. The error bars correspond to 1σ and vary according to the number of simulations in each mass bin.

Table 9. Mass ranges in M_{\oplus} unit from our simulations for each belt and the three positions of the A0 star, centered, at 30 per cent and 60 per cent of r_{in} , as in Table 8. Note how the three stellar positions give comparable results.

		Hot	Warm	Cold
Centered	10%	1.4×10^{-6}	9.0×10^{-4}	1.6×10^{-1}
	50%	2.9×10^{-5}	2.7×10^{-2}	3.5
	90%	2.0×10^{-3}	2.4	3.5×10^2
30% r_{in}	10%	1.1×10^{-6}	6.8×10^{-4}	1.6×10^{-1}
	50%	2.8×10^{-5}	2.4×10^{-2}	3.4
	90%	1.3×10^{-3}	1.8	4.4×10^2
60% r_{in}	10%	9.3×10^{-7}	5.9×10^{-4}	1.5×10^{-1}
	50%	2.3×10^{-5}	2.5×10^{-2}	2.5
	90%	2.8×10^{-3}	2.1	4.0×10^2

cold disks should be detectable in polarimetry at approximately our detection threshold, if their configurations are suitable.

4.3.2 Effect of the star's position

As explained above, to study the polarization from elliptical disks, we moved the position of the star from 0 per cent to 30 per cent and 60 per cent of r_{in} . These results are shown in Figure 5 for the A0 star as an example. Note that the sum of the three panels of Figure 5 corresponds to the top panel of Figure 4. As before, the masses correspond to a polarization of 1×10^{-4} . As we can see in Figure 5, there are slight differences between the three simulations but smaller than one order of magnitude in the mass of the belts. This is confirmed by comparing 10, 50 and 90 percentiles for the three belts and the three positions of the A0 star in Table 9 with each other and with those for the A0 star in Table 8. We also plotted cumulative distribution functions of the mass distributions for the belts considered in Table 9 (not shown here). The curves for the three stellar positions are very similar, with only minor differences, confirming our conclusions. Therefore, the stellar position is not as important as what one could expect. The explanation might be that

part of the disk causes a larger polarization because of its proximity, but other parts produce a smaller polarization, compared to a circular disk; hence the global effect is modest only. We can conclude that position of the star has a second order effect on the polarization when we have circular disks. This conclusion probably applies also to eccentric disks.

4.3.3 Parameter study

In Figures 4 and 5 we plot three parameters we considered for this study to understand their relative importance on the detectability of disks. Unfortunately, we can only see rough tendencies and not fine effects because of the discretization of the parameters' values. This

produces selection effects which we will try to determine in order to have contextualised results.

The effect of the surface density power-law index, $\alpha \in \{-3.5, -2.0, -0.5\}$, can be seen best for the hot and warm belts. As we could predict, sharper the disk is, smaller the mass needed will be. A sharp disk, i.e. with a high index implies that most of the mass will be closer to the star, which means more light to scatter for dust grains. This effect is not so clear for Kuiper belts since they are much farther from the star and so, the relative sprawl of the disk does not affect significantly the fraction of light received by the observer.

The minimum dust grain size, a_{min} , appears to be a critical element in the analysis: it confirms what we expected and is consistent with what was obtained with our toy model with only a single grain size (section 4.1): when the minimum size diminishes, the mass needed for polarization detection is smaller. It is due to the higher relative cross-section of tinier bodies compared to their mass. Therefore, when more tiny dust grains are available, more scattered, and polarized, light will be produced, implying an easier detection. But we tested only three values (10^{-1} , 1, 10) μm for this parameter. So, when we reach high masses, we notice a saturation effect. This is an effect due to the selection which is probably not physical: by introducing even bigger sizes, we might have seen that the plot continues to grow.

The size distribution power-law exponent, κ , acts the same way as the minimum size: it controls the number of tiny dust grains. The higher the exponent is, the tinier the grains will be (on average). So, obviously, the lowest detectable masses are those with the highest exponent which makes the size distribution sharper.

5 DISCUSSION

5.1 Interstellar polarization in the solar neighbourhood

Up until now, we purposely analysed the sample of stars as if their polarization is due entirely to debris disks. The fact that only two stars detected in polarization are associated with debris disks detected by mid- and far-IR excess (see section 3.1 and Table 1) suggests that something else is contributing to the polarization detected in these stars. Indeed, even if our sample stars are nearby, it is possible or likely that the detected polarization is due to interstellar dust aligned by magnetic fields. Leroy (1993b) used his polarization catalogue to confirm the previous result by Tinbergen (1982) about a significant depletion of dust within 35 pc from the Sun. Leroy (1999) updated his results when the *Hipparcos* distances became available and showed that previous distances had been underestimated. As a result, the cavity walls of our local bubble are located at 70 to 150 pc, varying with direction. In addition to not being spherical, the local bubble is hot, as X-rays have been detected (Snowden et al. 1990; Frisch et al. 2011). This means that our sample stars are all located *inside* the very low-density local bubble since their distances vary from up to 9 pc for M-type stars to up to 46 pc for A-type stars.

More recent observations with high precision polarimeters confirm the early observations. Bailey et al. (2010b) and Cotton et al. (2016a,b) presented surveys of nearby bright stars in the northern and southern hemispheres, respectively. They show that even in the low-density local bubble, the polarization increases linearly with distance as $P/d \sim 1 \times 10^{-6} \text{ pc}^{-1}$ (Cotton et al. 2016a,b), instead of $2 \times 10^{-5} \text{ pc}^{-1}$ in the general interstellar medium (Behr 1959) outside the local bubble. In the direction of the North Galactic pole, PlanetPol measured a value as low as $P/d \sim 2 \times 10^{-7} \text{ pc}^{-1}$

(Bailey et al. 2010b) inside our local bubble. Stars with a polarization compatible with this linear distance dependence ($\sim 1 \times 10^{-6} \text{ pc}^{-1}$) and aligned with other stars in similar directions on the sky would have a polarization compatible with interstellar polarization. Stars with different (larger) polarizations than given by this relation and orientation different than their neighbours' can be suspected of having a component of their polarization due to a debris disk.

The two stars with debris disks and detected polarization, HD 7570 and HD 165908, both have a linear polarization much higher than what these relations predict for a distance of 15 pc, $P/d \sim 49.6 \pm 4.0 \times 10^{-6} \text{ pc}^{-1}$ and $9.6 \pm 3.2 \times 10^{-6} \text{ pc}^{-1}$ respectively, and therefore cannot be explained by local interstellar polarization.

In Table 1 we present 16 other systems detected in polarization and without a FIR excess except one with an unknown status. We also computed their P/d ratio and all of them have a significant ratio, i.e. $P/d > 3\sigma$ and also $P/d > 1 \times 10^{-6} \text{ pc}^{-1}$, the expected linear polarization dependence within our local bubble. Therefore all of them are possible candidates to have an intrinsic polarization component which could be due to a debris disk not detected by their FIR excess yet (see also section 5.3). However, we caution that twelve of those 16 stars (not including HD 165908) have a detected polarization $3.0 < P/\sigma_p < 4.0$ and should be confirmed with high precision polarimeters.

5.2 Cold disks are more favourable for polarization detection

In section 4.3.1 above, we compared the model mass required to obtain a polarization equal to a polarization threshold of 10^{-4} to observed masses for the three different belt types and a range of typical spectral types. We found that observed masses of hot disks fall significantly (by factors of 100 to 1000) below masses corresponding to the polarization threshold; the mass a few warm disks barely reaches the masses of the threshold. However, many observed cold disks have masses above the masses required for the polarization threshold. The polarization threshold was chosen to correspond approximately to the limit that *traditional* polarimeters can reach in routine observations, although they can with great care exceed it somewhat (see, e.g., Table 1). It is now clear with the above comparison that essentially only the massive cold disks have a good chance to be detected with traditional polarimeters.

Naively, one might have expected to measure the polarization more easily for hot belts than for cold ones, since dust grains located in hot belts present a larger solid angle as seen from the star than dust grains farther out in cold disks because of their proximity to their star. Effectively, simulations show that smaller masses are required to obtain a polarization of 10^{-4} (Table 8) for hot disks than for warm and cold ones. But these results do not match with observations. Observed masses, as determined by fits to SEDs and resolved imaging data, are too small for hot disks, barely reach required masses for warm disks and are just about right for cold disks to be detected with unresolved polarimetry in the visible.

One way to explain this paradox is to use the two-parameter model of debris disks presented by Wyatt (2008). Such a simplification is possible because the SED of known debris disks can be represented reasonably well by a black body with a single temperature, T . The other parameter is the fractional luminosity, defined as the ratio of the IR luminosity of the dust to that of the star, $f = L_{IR}/L_*$. In his model, Wyatt (2008) shows that the disk mass expressed in M_{\oplus} is a scaled version of the fractional luminosity,

$$M_{disk} = 12.6 f r^2 \kappa_v^{-1} X_{\lambda}^{-1}, \quad (8)$$

where r is the disk radius in AU, the opacity $\kappa_v = 45 \text{ AU}^2 M_{\oplus}^{-1} (=$

$1.7 \text{ cm}^2 \text{ g}^{-1}$) at $850 \mu\text{m}$, and $X_\lambda = 1$ for $\lambda < 210 \mu\text{m}$ and $X_\lambda = \lambda/210$ otherwise. Rhee et al. (2007) have shown that $M_{\text{disk}}/f \propto r^2$ holds across the FIR and submm regimes. Since we know that disk mass is proportional to polarization (cf. equation 5), we get:

$$P \propto fr^2. \quad (9)$$

This equation shows that cold disks located further away than hot and warm disks should have a higher polarization. Also, disks with a higher fractional luminosity f are the best ones to observe as they should have a larger polarization. In fact, the fractional luminosity defines the total cross-sectional area of optically thin disks (Wyatt 2008): $\sigma_{\text{tot}} = 4\pi r^2 f$, where σ_{tot} is in AU^2 . Therefore, cold disks are more efficient at polarizing stellar light simply because they have more dust grains, hence more mass, than closer disks.

As pointed out by Krivov (2010), this simple model is not perfect since mass and polarization do not have the same dependence on the grain size distribution, $n(a)$. Mass hides mostly where $n(a)a^3$ is maximum and is affected by a_{max} , the maximum grain size, whereas polarization peaks approximately where $x = ka = 2\pi a/\lambda \approx 2$, where λ is the wavelength of observation. For our $0.76 \mu\text{m}$ data, this gives $a \approx 0.2 - 0.3 \mu\text{m}$, significantly smaller than grains contributing most of the detected mass, with $a \sim 1 \text{ mm}$ (e.g. Holland et al. (2017)). Despite this difference in the most sensitive grain radii for mass and polarization, the model does offer a rough understanding of the physics involved and helps understanding why cold disks have larger polarizations.

5.3 High precision polarimetry and polarization detection

High precision polarimeters have begun to observe stars with debris disks (Bailey et al. 2010b; Cotton et al. 2016a,b; Marshall et al. 2016) and indeed can measure their polarization. So far, 15 stars with known debris disks and two with IR excess have been observed with high precision polarimeters and the data published. Bailey et al. (2010b) observed 6 of them and discussed the results for Vega in detail. Its polarization is $17.2 \pm 1.0 \text{ ppm}$ (10^{-6}). However its debris disk extends from 11 arcsec to 105 arcsec according to *Spitzer* observations (Su et al. 2005) and was therefore outside the aperture of PlanetPol. There is also evidence for circumstellar material within 1 arcsec, probably a hot disk. However the disk is seen essentially face-on ($i = 4.7^\circ$) hence the authors conclude that its polarization is compatible with being entirely of interstellar origin. Their five other debris disk stars are discussed by Cotton et al. (2016a,b). Merak ($\beta \text{ UMa}$) and $\beta \text{ Leo}$ are compatible with an interstellar origin and probably also $\alpha \text{ CrB}$ but this last one is also an Algol-type eclipsing binary. The best case is $\gamma \text{ Oph}$ which has a polarization of 40 ppm but given its distance of 29 pc, its polarization is compatible with an interstellar origin. However its polarization angle is aligned with the minor axis of the imaged disk (Cotton et al. 2016a,b), the expected polarization orientation. It is therefore likely that $\gamma \text{ Oph}$ has two polarization components, intrinsic and interstellar. Marshall et al. (2016) observed 6 stars with strong excess at NIR wavelengths, an indicator of hot dust belts, and did not detect the expected strong polarization in any of them. They ruled out scattered light as the origin of their emission as the probability of all six of them being seen face-on is small. The results of our simulations presented above show that the level of polarization expected for hot belts are difficult to observe, even with high precision polarimeters.

With the performances of high precision polarimeters, we can certainly detect some debris disks in polarimetry. If a polarization

level of 10^{-4} was high enough to reject easily or neglect the interstellar component of the polarization in the past, this is not the case for polarizations as low as 10^{-6} . Cotton et al. (2016a,b) analysed the interstellar polarization inside the solar bubble and concluded that, depending on the direction observed, the polarization increase with distance is between 2×10^{-7} and $2 \times 10^{-6} \text{ pc}^{-1}$. The lowest rate found in our detected measurements in Table 1 is $(5 \pm 1) \times 10^{-6} \text{ pc}^{-1}$. So, all the polarizations detected are above the level of interstellar polarization in the solar bubble by at least a factor of 2 and are therefore likely to have an intrinsic polarization component. With the lower polarization levels reached by the new polarimeters, disentangling interstellar and intrinsic debris-disk polarizations is now a real issue to be considered. This is particularly the case for stars located near the galactic plane. One way to address this issue is to take measurements in different filters to obtain the wavelength dependence of the polarization and compare with the expected dependence of the interstellar polarization. If there are significant deviations from Serkowski's law, and in particular if the observed polarization angles rotate as a function of wavelength, then a least-squares fit method can be used to separate the two components, as done by Poeckert et al. (1979) for classical Be stars. Such a method works if the two polarization components, intrinsic and interstellar, are not collinear in the Stokes Q - U plane, and if the data are of sufficient quality. Since this method will be more time consuming, it will be appropriate for studying a few stars at a time, not for a large survey.

We showed in section 3.2 that there is no statistically significant difference between samples with debris disks and those without, according to KS tests and their cumulative distribution functions. García & Gómez (2015) observed 88 southern hemisphere stars, with and without mid-IR excess based on *Spitzer* observations and with aperture polarimetry in 4 different filters. They combined their sample with an earlier version of ours, Simon (2010), selecting stars with and without known debris disks, based on IR excess emission, and removing stars with unknown status. With their 51 IR-excess stars and 97 stars without IR excess, they found similar results with their CDF and statistical analyses than ours.

6 CONCLUSION AND FURTHER PROSPECTS

We performed a coherent census of polarization due to nearby debris disks for 109 stars. The stars were selected from the DEBRIS and DUNES candidate stars observed with *Herschel*. Combining with polarization measurements from the literature for other candidate stars, we obtained a list of 223 stars with also information about the presence of debris disks based on their mid- and far-IR excesses. Eighteen of them were detected with a polarization $P \geq 3\sigma_p$. We found that the polarization distribution of the samples with and without debris disks are not statistically different. Among the eighteen stars with detected polarization, two of them have a debris disk according to their IR excesses. One of them, HD 165908 is a binary with an imaged disk; its polarization is parallel to the pericentre direction, within a few degrees, as expected. The other star, HD 7570, is single and has not been imaged yet, hence we predict the orientation of its disk, position angle $\approx 138^\circ$, perpendicular to its strong polarization.

There are many factors which can explain the low-detection rate result, separately or in combination:

1. Only about 20 per cent of stars have one or more debris disks according to their mid-IR and FIR excesses (Eiroa et al. 2013; Rodriguez et al. 2015b; Montesinos et al. 2016);

2. The dust mass present may not be sufficient to produce a detectable polarization, or equivalently the fractional luminosity of the disk is too small (see sections 4.3 and 5.2);
3. The inclination of the disk may be such that the polarization as seen by the observer cancels out (mostly face-on disks);
4. Disks around some stars are too large to fit within the aperture used by polarimeters (e.g., the case of α Lyr discussed above);
5. Dust grains may not be good scatterers in visible bands, such as nano-scale size dust grains trapped in hot belts (Marshall et al. 2016; García & Gómez 2015; Rieke et al. 2016).

Factor 2 above (insufficient dust) can be mostly overcome with high precision polarimeters. One can use a larger diaphragm to solve factor 4, to some extent, as long as there is no background star within the larger aperture. As discussed above, interstellar polarization needs to be accounted for in the analysis of the polarization data.

The analytical model and numerical simulations are consistent with observational results. We computed mass histograms corresponding to a polarization threshold of 10^{-4} for cold, warm and hot disks with a large grid of model parameters. Comparison with masses obtained from observations of IR excesses shows that simulated hot belts yield masses larger than the observed ones by up to a factor of 1000. The masses of only a few warm disks observed by *Spitzer* reach those of models corresponding to the polarization of 10^{-4} . However, this polarization level produces disk masses reached and exceeded by many cold disks as seen by the JCMT/SCUBA-2 SONS survey (Holland et al. 2017). These simulations show that cold disks can be detected by traditional polarimeters, but high precision polarimeters are needed for detection of warm and hot disks. Of course, the caveats or factors mentioned above apply.

This result can be explained by the fact that polarization $P \propto f r^2 \propto \sigma_{tot}$, the total cross-sectional area of dust grains in optically thin disks, as derived from the two-parameter debris disk model (section 5.2). Cold disks have a larger polarization because they have more dust grains and more mass than closer disks.

The simulations also showed that eccentric disks have only minor effects on the level of polarization, at least as much as represented by moving the position of the star interior to circular disks. The effect of the slope of the surface density distribution is better seen in hot and warm disks. The larger the slope, the smaller the mass needed to produce a given polarization. With the limitation of only three minimum grain sizes, more scattered and polarized light is produced when the minimum grain size is reduced. This can be explained by the higher relative cross sections of small grains for a given mass. Finally, the slope of the size distribution acts in the same manner: more small grains means higher polarization.

ACKNOWLEDGEMENTS

The authors wish to sincerely thank the telescope operators at the Mont-Mégantic Observatory, Pierre-Luc Lévesque, Bernard Malenfant and Ghislain Turcotte. We also would like to thank Rémi Fahed, Patrick Ingraham and Lison Malo for their precious help, Marie-Michèle Limoges for a careful reading of a previous version of this manuscript and David Lafrenière for insightful discussions about HR 8799. We thank the anonymous referee whose constructive comments and requests have helped improve significantly the paper. This research was supported in part by a grant from the Conseil de Recherche en Sciences Naturelles et en Génie du Canada. J.-C. A. acknowledges support from the Programme National de

Planétologie (PNP) of CNRS/INSU co-funded by the CNES. This research has made use of the SIMBAD database and the VizieR catalog access tool, operated at CDS, Strasbourg, France.

REFERENCES

- Absil O., et al., 2006, *A&A*, 452, 237
 Absil O., et al., 2008, *A&A*, 487, 1041
 Acke B., et al., 2012, *A&A*, 540, A125
 Allen C. W., 1973, *Astrophysical Quantities*. Athlone Press, University of London
 Appenzeller I., 1968, *ApJ*, 151, 907
 Backman D. E., Paresce F., 1993, in Levy E. H., Lunine J. I., eds, *Protostars and Planets III*, Univ. of Arizona Press, Tucson, AZ. pp 1253–1304
 Bailey J., Lucas P. W., Hough J. H., 2010a, *MNRAS*, 405, 2570
 Bailey J., Lucas P. W., Hough J. H., 2010b, *VizieR Online Data Catalog*, 740
 Bastien P., 1987, *ApJ*, 317, 231
 Behr A., 1959, *Vereöffentlichungen der Universitaets-Sternwarte zu Goettingen*, 7, 200.1
 Beichman C. A., et al., 2005, *ApJ*, 622, 1160
 Beichman C. A., et al., 2006a, *ApJ*, 639, 1166
 Beichman C. A., et al., 2006b, *ApJ*, 652, 1674
 Bhatt H. C., 1996, *A&AS*, 120, 451
 Bhatt H. C., Manoj P., 2000, *A&A*, 362, 978
 Bohren C. F., Huffman D. R., 1998, *Absorption and Scattering of Light by Small Particles*. Wiley-VCH, New-York
 Boley A. C., Payne M. J., Corder S., Dent W. R. F., Ford E. B., Shabram M., 2012, *ApJ*, 750, L21
 Brown J. C., McLean I. S., Emslie A. G., 1978, *A&A*, 68, 415
 Burgasser A. J., Kirkpatrick J. D., Reid I. N., Brown M. E., Miskey C. L., Gizis J. E., 2003, *ApJ*, 586, 512
 Chavero C., Gómez M., Whitney B. A., Saffe C., 2006, *A&A*, 452, 921
 Cotten T. H., Song I., 2016, *ApJS*, 225, 15
 Cotton D. V., Bailey J., Kedziora-Chudczer L., Bott K., Lucas P. W., Hough J. H., Marshall J. P., 2016a, *MNRAS*, 455, 1607
 Cotton D. V., Bailey J., Kedziora-Chudczer L., Bott K., Lucas P. W., Hough J. H., Marshall J. P., 2016b, *MNRAS*, 460, 18
 Defrère D., et al., 2011, *A&A*, 534, A5
 Draine B. T., 1985, *ApJS*, 57, 587
 Eiroa C., et al., 2013, *A&A*, 555, A11
 Eritsyan M. A., Hovhannessian R. K., Hovhannessian E. R., 2002, *Astrophysics*, 45, 25
 Ertel S., Wolf S., Rodmann J., 2012, *A&A*, 544, A61
 Faramaz V., et al., 2014, *A&A*, 563, A72
 Fixsen D. J., Dwek E., 2002, *ApJ*, 578, 1009
 Frisch P. C., Redfield S., Slavin J. D., 2011, *ARA&A*, 49, 237
 García L., Gómez M., 2015, *Rev. Mex. Astron. Astrofis.*, 51, 3
 Gáspár A., Rieke G. H., Balog Z., 2013, *ApJ*, 768, 25
 Gáspár A., Rieke G. H., Ballering N., 2016, *ApJ*, 826, 171
 Gledhill T. M., Scarrott S. M., Wolstencroft R. D., 1991, *MNRAS*, 252, 50P
 Graham J. R., Kalas P. G., Matthews B. C., 2007, *ApJ*, 654, 595
 Gray R. O., Corbally C. J., Garrison R. F., McFadden M. T., Robinson P. E., 2003, *AJ*, 126, 2048
 Hauschildt P. H., Allard F., Baron E., 1999, *ApJ*, 512, 377
 Heiles C., 2000, *AJ*, 119, 923
 Holland W. S., et al., 2017, *MNRAS*, 470, 3606
 Hough J. H., Lucas P. W., Bailey J. A., Tamura M., Hirst E., Harrison D., Bartholomew-Biggs M., 2006, *PASP*, 118, 1302
 Huovelin J., Pirola V., 1990, *A&A*, 231, 588
 Huovelin J., Linnaluoto S., Pirola V., Tuominen I., Virtanen H., 1985, *A&A*, 152, 357
 Huovelin J., Saar S. H., Tuominen I., 1988, *ApJ*, 329, 882
 Kennedy G. M., et al., 2012, *MNRAS*, 421, 2264

- Kirchschlager F., Wolf S., Krivov A. V., Mutschke H., Brunngräber R., 2017, *MNRAS*, 467, 1614
- Korhonen T., Reiz A., 1986, *A&AS*, 64, 487
- Kóspál Á., Ardila D. R., Moór A., Ábrahám P., 2009, *ApJ*, 700, L73
- Krautter J., 1980, *A&AS*, 39, 167
- Krivov A. V., 2010, *Research in Astronomy and Astrophysics*, 10, 383
- Krivova N. A., Krivov A. V., Mann I., 2000, *ApJ*, 539, 424
- Lawler S. M., et al., 2009, *ApJ*, 705, 89
- Lebreton J., et al., 2012, *A&A*, 539, A17
- Lebreton J., et al., 2013, *A&A*, 555, A146
- Leroy J. L., 1993a, *A&AS*, 101, 551
- Leroy J. L., 1993b, *A&A*, 274, 203
- Leroy J. L., 1999, *A&A*, 346, 955
- Leroy J. L., Landolfi M., Landi Degl'Innocenti E., 1993, *A&A*, 270, 335
- Lestrade J.-F., Wyatt M. C., Bertoldi F., Dent W. R. F., Menten K. M., 2006, *A&A*, 460, 733
- Lucas P. W., Hough J. H., Bailey J. A., Tamura M., Hirst E., Harrison D., 2009, *MNRAS*, 393, 229
- Maldonado J., Eiroa C., Villaver E., Montesinos B., Mora A., 2015, *VizieR Online Data Catalog*, 357
- Manset N., 2005, in Adamson A., Aspin C., Davis C., Fujiyoshi T., eds, *Astronomical Society of the Pacific Conference Series Vol. 343, Astronomical Polarimetry: Current Status and Future Directions*, Astron. Soc. Pac., San Francisco, p. 389 (arXiv:astro-ph/0511204)
- Manset N., Bastien P., 1995, *PASP*, 107, 483
- Marois C., Macintosh B., Barman T., Zuckerman B., Song I., Patience J., Lafrenière D., Doyon R., 2008, *Science*, 322, 1348
- Marois C., Zuckerman B., Konopacky Q. M., Macintosh B., Barman T., 2010, *Nature*, 468, 1080
- Marshall J. P., et al., 2014, *A&A*, 565, A15
- Marshall J. P., et al., 2016, *ApJ*, 825, 124
- Mathewson D. S., Ford V. L., 1970, *Mem. RAS*, 74, 139
- Matthews B. C., et al., 2007, *PASP*, 119, 842
- Matthews B. C., et al., 2010, *A&A*, 518, L135
- Matthews B. C., Krivov A. V., Wyatt M. C., Bryden G., Eiroa C., 2014, *Protostars and Planets VI*, Univ. Arizona Press, Tucson, AZ, pp 521–544
- Montesinos B., et al., 2016, *A&A*, 593, A51
- Najita J., Williams J. P., 2005, *ApJ*, 635, 625
- Nesvorný D., Jenniskens P., Levison H. F., Bottke W. F., Vokrouhlický D., Gounelle M., 2010, *ApJ*, 713, 816
- Oudmajer R. D., et al., 2001, *A&A*, 379, 564
- Panić O., et al., 2013, *MNRAS*, 435, 1037
- Phillips N. M., Greaves J. S., Dent W. R. F., Matthews B. C., Holland W. S., Wyatt M. C., Sibthorpe B., 2010, *MNRAS*, 403, 1089
- Phillips N. M., Greaves J. S., Dent W. R. F., Matthews B. C., Holland W. S., Wyatt M. C., Sibthorpe B., 2012, *VizieR Online Data Catalog*, 740
- Pirola V., 1977, *A&AS*, 30, 213
- Pinte C., Ménard F., Duchêne G., Bastien P., 2006, *A&A*, 459, 797
- Plets H., Vynckier C., 1999, *A&A*, 343, 496
- Poeckert R., Bastien P., Landstreet J. D., 1979, *AJ*, 84, 812
- Reidemeister M., Krivov A. V., Schmidt T. O. B., Fiedler S., Müller S., Löhne T., Neuhäuser R., 2009, *A&A*, 503, 247
- Rhee J. H., Song I., Zuckerman B., McElwain M., 2007, *ApJ*, 660, 1556
- Rieke G. H., Gáspár A., Ballering N. P., 2016, *ApJ*, 816, 50
- Rodríguez D. R., Duchêne G., Tom H., Kennedy G. M., Matthews B., Greaves J., Butner H., 2015a, *MNRAS*, 449, 3160
- Rodríguez D. R., van der Plas G., Kastner J. H., Schneider A. C., Faherty J. K., Mardones D., Mohanty S., Principe D., 2015b, *A&A*, 582, L5
- Schneider G., Becklin E. E., Smith B. A., Weinberger A. J., Silverstone M., Hines D. C., 2001, *AJ*, 121, 525
- Schneider G., et al., 2014, *AJ*, 148, 59
- Schröder R., 1976, *A&AS*, 23, 125
- Serkowski K., 1962, *Advances in Astronomy and Astrophysics*, 1, 289
- Serkowski K., 1970, *ApJ*, 160, 1083
- Simmons J. F. L., 1982, *MNRAS*, 200, 91
- Simon A., 2010, M.Sc. thesis, Univ. Montréal
- Snowden S. L., Cox D. P., McCammon D., Sanders W. T., 1990, *ApJ*, 354, 211
- Su K. Y. L., et al., 2005, *ApJ*, 628, 487
- Su K. Y. L., et al., 2009, *ApJ*, 705, 314
- Tamura M., Fukagawa M., 2005, in Adamson A., Aspin C., Davis C., Fujiyoshi T., eds, *Astronomical Society of the Pacific Conference Series Vol. 343, Astronomical Polarimetry: Current Status and Future Directions*, Astron. Soc. Pac., San Francisco, p. 215
- Tamura M., Fukagawa M., Kimura H., Yamamoto T., Suto H., Abe L., 2006, *ApJ*, 641, 1172
- Tanner A., Beichman C., Bryden G., Lisse C., Lawler S., 2009, *ApJ*, 704, 109
- Thébaud P., Augereau J.-C., 2007, *A&A*, 472, 169
- Tinbergen J., 1982, *A&A*, 105, 53
- Turnshek D. A., Bohlin R. C., Williamson II R. L., Lupie O. L., Koornneef J., Morgan D. H., 1990, *AJ*, 99, 1243
- Walborn N. R., 1968, *PASP*, 80, 162
- Wiktorowicz S., Graham J. R., Duchene G., Kalas P., 2010, in *American Astronomical Society Meeting Abstracts #215*, p. 582
- Williams D. R., Wetherill G. W., 1994, *Icarus*, 107, 117
- Wolstencroft R. D., Scarrott S. M., Gledhill T. M., 1995, *Ap&SS*, 224, 395
- Wyatt M. C., 2008, *ARA&A*, 46, 339
- Wyatt M. C., Dent W. R. F., 2002, *MNRAS*, 334, 589
- Wyatt M. C., Dent W. R. F., Greaves J. S., 2003, *MNRAS*, 342, 876
- di Folco E., et al., 2007, *A&A*, 475, 243

APPENDIX A: ALL STARS FROM THE SAMPLE WITH A POLARIZATION $P < 3\sigma_p$

We present in Table A1 below stars in our sample with a polarization $P < 3\sigma_p$. Stars with a detected polarization, $P \geq 3\sigma_p$, are given in Table 1. The polarization data for the sample stars come from OMM and from the Leroy compilation. The description of these two tables is given in section 3.

Table A1. Polarization data for all the stars observed at OMM and from the Leroy compilation with a polarization $P < 3\sigma_P$.

UNS ID	name	P (10^{-5})	σ_P (10^{-5})	$\theta(^{\circ})$	$\sigma_{\theta} (^{\circ})$	P/σ_P	Distance (pc)	FIR ^a excess	Observer ^b	Date ^c
M003	HD 95735	47	31	177	23	1.5	2.543±0.001	N	SI	02 Mar
M015	HIP 36208	11	30	26	34	0.4	3.795±0.018	?	SI	02 Mar
M031	HIP 54211	32	35	ind. ^d	52	0.9	4.862±0.022	?	SI	02 Mar
M032	GJ 388	78	50	54	15.	1.6	4.888±0.067	?	SI	23 Jan
M040	HD 119850	116	93	79.	20	1.2	5.395±0.030	N	SI	22 Jan
M042	HD 265866	0	36	ind.	52	0.0	5.614±0.04	N	SI	21 Jan
M053	HIP 37766	0	31	130	44	0.0	5.982±0.073	?	SI	02 Ma.
M054	HIP 34603	0	46	ind.	52	0.0	6.119±0.067	?	SI	22 Jan
M060	GJ 661 A	54	44	144	20	1.2	6.397±0.052	?	SI	02 Mar
M067	HIP 53767	0	30	ind.	52	0.0	6.697±0.071	?	SI	02 Mar
M069	GJ 3522	103	36	79.	11.	2.8	6.772±0.09	?	SI	02 Mar
M070	HIP 53020	54	41	75	18	1.3	6.794±0.137	?	SI	02 Mar
M076	HIP 51317	20	37	144	23	0.5	7.129±0.103	?	SI	02 Mar
M090	GJ 1093	170	120	57	19	1.4	7.764±0.211	?	SI	22 Jan
M095	HIP 49986	56	34	152	22	1.6	7.930±0.114	?	SI	02 Mar
M100	HIP 86287	0	33	ind.	52	0.0	8.050±0.097	?	SI	02 Mar
M110	GJ 1230 A	83	50	ind.	ind.	1.7	8.271±0.493	?	SI	02 Mar
M109	HIP 38956	31	45	ind.	52	0.7	8.269±0.159	?	SI	22 Jan
K005	HD 88230	82	48	160	19	1.7	4.866±0.012	?	SI	22 Jan
K011	HD 79210	14	40	118	22	0.4	6.108±0.094	N	SI	08 Dec
K014	HD 16160	14	13	ind.	ind.	1.1	7.191±0.023	N	LE	
K016	HD 4628	32	11	ind.	ind.	2.9	7.449±0.027	N	SC LE	
K017	HD 10476	16	6	166	19	2.7	7.533±0.028	N	SI SE MA	23 Jan
K019	HD 216803	7	18	ind.	ind.	0.4	7.611±0.036	N	SC	
K021	HD 157881	33	33	ind.	52	1.0	7.700±0.042	?	SI	02 Mar
K027	HD 192310	10	13	ind.	ind.	0.8	8.910±0.024	N	LE	
K028	HD 103095	9	37	177	21	0.2	9.081±0.033	?	SI AP	22 Jan
K031	HD 151288	59	35	81	18	1.7	9.809±0.067	N	SI	02 Mar
K041	HIP 66459	66	36	96	12	1.8	10.935±0.135	?	SI	02 Mar
K055	15009+4526A	65	38	125	15.	1.7	11.881±0.147	?	SI	02 Mar
K056	HD 97101	53	24	135.	10.	2.2	11.961±0.120	?	SI	04 Dec
K060	HD 75732	99	42	136.	11.	2.4	12.460±0.104	?	SI	21 Jan
K064	HD 82106	31	32	ind.	52	1.0	12.894±0.106	?	SI	02 Mar
K070	HIP 67090	52	41	57	16	1.3	13.193±0.169	?	SI	22 Jan
K072	HD 128165	0	37	175	48	0.0	13.215±0.073	?	SI	02 Mar
K074	HD 120476	12	33	ind.	52	0.4	13.373±0.136	?	SI	02 Mar
K082	HIP 27188	0	30	ind.	52	0.0	13.716±0.176	?	SI	21 Jan
K086	GJ 400 A	70	29	132.	13.	2.4	13.900±0.316	?	SI	04 Dec
K092	HD 110315	98	49	88.	14.	2.0	14.194±0.146	?	SI	22 Jan
K096	HIP 70218	35	36	ind.	52	1.0	14.393±0.169	?	SI	02 Mar
K098	HD 144579	0	46	ind.	52	0.0	14.508±0.069	?	SI	02 Mar
K099	HIP 37288	0	31	ind.	52	0.0	14.533±0.292	?	SI	02 Mar
K108	HIP 13375	0	64	ind.	52	0.0	14.757±0.299	?	SI	23 Jan
K111	HD 110833	0	33	ind.	52	0.0	14.889±0.146	?	SI	02 Mar
K121	GJ 319 A	0	29	105	28	0.0	15.368±0.399	?	SI	02 Mar
G005	HD 20794	3	6	ind.	ind.	0.5	6.043±0.007	Y	SC TI KO MA	
G006	HD 131156	8	8	ind.	ind.	1.0	6.708±0.021	N	LE HU	
G007	HD 109358	15	7	67	34	2.1	8.440±0.014	N	SI PI TI BE	02 Mar
G008	HD 115617	10	6	ind.	ind.	1.7	8.555±0.016	Y	SE TI LE MA	
G010	HD 114710	2	4	ind.	ind.	0.5	9.132±0.014	N	PI TI SE HU	
G011	HD 20630	6	6	ind.	ind.	1.0	9.144±0.022	N	SC TI HU LE	
G012	HD 102365	21	8	ind.	ind.	2.6	9.221±0.020	N	TI MA	
G016	HD 13974	17	7	51	24	2.4	10.778±0.045	N	SI TI PI BE	23 Jan
G017	HD 82885	17	8	ind.	ind.	2.1	11.363±0.041	N	PI LE BE	
G019	HD 141004	1	7	ind.	ind.	0.1	12.122±0.045	N	TI LE BE	
G025	HD 133640	20	31	ind.	52	0.6	12.740±0.097	N	SI	02 Mar
G026	HD 10307	13	10	ind.	ind.	1.3	12.739±0.044	N	PI TI BE	
G029	HD 30495	7	11	129	18	0.6	13.273±0.063	N	SI LE	08 Dec
G033	HD 95128	35	12	ind.	52	2.9	14.062±0.049	?	SI TI	04 Dec
G040	HD 86728	7	11	ind.	52	0.6	15.052±0.071	?	SI LE	22 Jan

Table A1 – *continued* Polarization data for all the stars observed at OMM and from the Leroy compilation with a polarization $P < 3\sigma_P$.

UNS ID	name	P (10^{-5})	σ_P (10^{-5})	$\theta(^{\circ})$	$\sigma_{\theta(^{\circ})}$	P/σ_P	Distance (pc)	FIR ^a excess	Observer ^b	Date ^c
G057	HD 111395	18	23	18	20	0.8	16.938±0.129	?	SI AP	23 Jan
G061	HD 122742	29	10	38	13.	2.9	16.965±0.178	?	SI LE	22 Jan
G065	HD 50692	5	13	54	19	0.4	17.237±0.122	?	SI LE	21 Jan
G067	HD 142267	20	30	ind.	ind.	0.7	17.349±0.163	N	MA	
G079	HD 99491	9	16	ind.	ind.	0.6	17.777±0.210	N	LE	
G081	HD 137108	12	35	ind.	52	0.3	17.923±0.251	?	SI	02 Mar
G086	HD 84737	13	11	106	15.	1.2	18.344±0.094	N	SI LE	04 Dec, 22 Jan
G087	HD 222335	28	24	ind.	ind.	1.2	18.578±0.217	N	SC	
G088	HD 154345	0	55	ind.	52	0.0	18.582±0.110	?	SI	02 Mar
G089	HD 4747	39	22	ind.	ind.	1.8	18.672±0.188	N	SC	
G092	HD 9540	30	19	ind.	ind.	1.6	19.034±0.166	N	SC	
G093	HD 52711	11	13	176	17.	0.8	19.163±0.150	?	SI LE	21 Jan
G094	HD 78366	166	75	150.	14.	2.2	19.183±0.121	?	SI	21 Jan
G096	HD 43587	23	14	ind.	ind.	1.6	19.250±0.148	N	LE	
G100	HD 79028	20	25	ind.	52	0.8	19.569±0.122	?	SI LE	22 Jan
G101	HD 136923	29	30	ind.	52	1.0	19.600±0.242	N	SI	02 Mar
G107	HD 212698	15	11	ind.	ind.	1.4	20.191±0.487	N	SC	
G108	HD 89269	46	52	177	22	0.9	20.243±0.205	N	SI	22 Jan
G109	GJ 337 A	118	61	118	17.	1.9	20.369±0.227	?	SI	23 Jan
G113	HD 212330	4	8	ind.	ind.	0.5	20.569±0.144	N	SC	
G117	HD 197076	23	15	ind.	ind.	1.5	20.896±0.206	N	LE	
G118	HD 1835	11	7	ind.	ind.	1.6	20.923±0.229	N	LE SC	
G121	HD 117043	27	14	ind.	ind.	1.9	21.160±0.139	N	LE	
G122	HD 146361	7	8	ind.	ind.	0.9	21.196±0.485	N	LE	
F001	HD 61421	5	8	ind.	ind.	0.6	3.507±0.013	?	TI SE SP	
F003	HD 30652	13	9	ind.	ind.	1.4	8.069±0.011	N	PI TI BE	
F004	HD 98231	70	32	28.	15.	2.2	8.368±0.055	N	SI	04 Dec
F005	HD 1581	6	5	ind.	ind.	1.2	8.586±0.012	N	TI MA	
F006	HD 38393	2	6	ind.	ind.	0.3	8.926±0.014	Y	LE SE TI MA+	
F007	HD 203608	15	7	ind.	ind.	2.1	9.261±0.016	N	TI	
F011	HD 142860	13	7	ind.	ind.	1.9	11.255±0.023	N	TI MA LE	
F012	HD 33262	14	8	ind.	ind.	1.8	11.645±0.024	Y	TI	
F014	HD 110379	23	8	ind.	ind.	2.9	11.745±0.080	N	TI BE	
F015	HD 207098	14	6	ind.	ind.	2.3	11.869±0.02	N	WA TI	
F018	HD 90839	9	7	ind.	52	1.3	12.785±0.047	?	SI PI TI+ BE	04 Dec
F019	HD 82328	2	6	ind.	52	0.3	13.481±0.024	N	SI PI TI BE LE	22 Jan
F022	HD 22484	20	7	10	24	2.9	13.977±0.105	Y	SI TI	23 Jan
F023	HD 20010	6	9			0.7	14.235±0.091	N	SC	
F024	HD 17206	11	5	170	14.	2.2	14.237±0.365	N	SI SC TI BM	23 Jan
F026	HD 126660	9	12	ind.	ind.	0.8	14.528±0.030	N	PI TI BE	
F027	HD 197692	17	7	ind.	ind.	2.4	14.677±0.058	N	TI LE MA	
F030	HD 105452	12	8	ind.	ind.	1.5	14.936±0.036	N	TI	
F036	HD 120136	79	38	74.	15.	2.1	15.622±0.049	?	SI	22 Jan
F039	HD 128167	14	7	ind.	ind.	2.0	15.828±0.065	N	PI TI BE BM	
F043	HD 215648	8	4	ind.	ind.	2.0	16.296±0.053	N	SC PI BE MA	
F044	HD 48682	5	10	139	29	0.5	16.714±0.084	?	SI LE	04 Dec
F045	HD 55575	9	10	161	22	0.9	16.889±0.094	?	SI LE	22 Jan
F046	HD 17051	7	7	ind.	ind.	1.0	17.168±0.065	N	KO SC MA	
F048	HD 81997	20	30	ind.	ind.	0.7	17.313±0.602	N	MA	
F053	HD 23754	6	7	ind.	ind.	0.9	17.609±0.059	N	TI	
F055	HD 114378	24	13	48	32	1.8	17.828±0.282	N	SI LE HU AP	22 Jan
F058	HD 58946	18	7	11	19	2.6	18.022±0.078	N	SI PI TI BE	22 Jan
	GJ274	23	35	ind.	52	0.6	18.047±0.039	?	SI	08 Dec
F061	HD 69897	2	14	126	21	0.1	18.268±0.107	?	SI LE	21, 22, 23 Jan
F062	HD 129502	11	7	ind.	ind.	1.6	18.282±0.067	N	TI LE MA	
F063	HD 109085	11	16	ind.	ind.	0.7	18.282±0.060	Y	LE BM	
F066	HD 202275	8	6	ind.	ind.	1.3	18.218±0.083	N	WA TI LE	
F067	HD 56986	46	16	147	15.	2.9	18.515±0.228	N	SI BE	21, 22 Jan
F084	GJ 335 B	54	54	171	37	1.0	20.378±0.153	N	SI	22 Jan
	HD 78154	33	12	ind.	ind.	2.7	520.378±0.153	N	TI	
F085	HD 27290	22	8	ind.	ind.	2.8	20.461±0.151	Y	TI	

Table A1 – *continued* Polarization data for all the stars observed at OMM and from the Leroy compilation with a polarization $P < 3\sigma_P$.

UNS ID	name	P (10^{-5})	σ_P (10^{-5})	$\theta(^{\circ})$	$\sigma_{\theta(^{\circ})}$	P/σ_P	Distance (pc)	FIR ^a excess	Observer ^b	Date ^c
F090	HD 33564	12	11	179.	26	1.1	20.886±0.092	?	SI LE	21 Jan
F092	HD 3196	13	7	ind.	ind.	1.9	21.109±0.300	N	SC	
F096	HD 739	8	8	ind.	ind.	1.0	21.281±0.122	N	SC	
F097	HD 89449	5	2	ind.	52	2.5	21.372±0.110	N	SI PI TI BE	23 Jan.
F099	HD 160032	50	30	ind.	ind.	1.7	21.447±0.152	Y	MA	
F101	HD 22001	7	8	ind.	ind.	0.9	21.681±0.056	Y	TI	
F102	HD 16673	24	12	ind.	ind.	2.0	21.763±0.194	N	LE	
F103	HD 108954	54	42	12	16	1.3	21.782±0.166	N	SI	23 Jan
F106	HD 206826	6	11	ind.	ind.	0.5	22.204±0.211	N	LE	
F108	HD 106516	4	12	ind.	ind.	0.3	22.336±0.404	N	LE	
F109	HD 68146	0	30	ind.	ind.	0.0	22.377±0.150	N	MA	
F111	HD 213845	9	8	ind.	ind.	1.1	22.681±0.134	N	SC	
F112	HD 16765	21	12	ind.	ind.	1.8	22.687±0.428	N	SC	
F113	HD 89125	12	13	151	11.	0.9	22.789±0.181	N	SI LE	23 Jan
F114	HD 168151	15	10	ind.	ind.	1.5	22.906±0.089	N	LE	
F115	HD 162003	28	17	ind.	ind.	1.6	22.918±0.177	N	LE	
F117	HD 219571	5	5	ind.	ind.	1.0	23.066±0.335	N	SC	
F118	HD 160922	14	16	ind.	ind.	0.9	23.165±0.091	N	LE	
F119	HD 11171	16	6	ind.	ind.	2.7	23.175±0.139	Y	SC	
F120	HD 101177	145	49	45.	10.	2.9	23.195±0.391	N	SI	22 Jan
F121	HD 100180	124	63	47.	17.	2.2	3.326±0.658	N	SI	08 Dec
F122	HD 7439	5	7	ind.	ind.	0.7	23.375±0.164	Y	SC AP	
F124	HD 4676	3	23	ind.	ind.	0.1	23.451±0.148	N	LE	
F126	HD 214953	25	15	ind.	ind.	1.7	23.621±0.223	N	SC BM	
A002	HD 187642	7	6	ind.	ind.	1.2	5.125±0.014	N	PI SC TI BE	
A005	HD 102647	6	7	ind.	ind.	0.9	11.011±0.063	Y	TI PI BE BM	
A006	HD 60179	67	25	179.	10.	2.7	14.005±0.408	N	SI	08 Dec
A007	HD 76644	24	11	93	28	2.2	14.509±0.034	N	SI LE	08 Dec
A011	HD 97603	7	7	175	20	1.0	17.918±0.080	N	SI PI TI BE	23 Jan
A012	HD 11636	12	5	ind.	ind.	2.4	17.965±0.187	N	PI TI BE	
A013	HD 115892	11	7	ind.	ind.	1.6	18.021±0.055	N	TI BM	
A015	HD 141795	16	12	ind.	ind.	1.3	21.610±0.089	N	LE	
A016	HD 38678	11	8	131	26	1.4	21.612±0.075	Y	SI TI	08 Dec
A018	HD 139006	14	6	ind.	ind.	2.3	23.007±0.148	Y	PI BE+ BM	
A019	HD 156164	18	29	ind.	ind.	0.6	23.038±0.080	N	BE	
A021	HD 2262	10	5	ind.	ind.	2.0	23.807±0.091	Y	TI MA	
A023	HD 16970	5	14	ind.	ind.	0.4	24.348±0.367	N	LE	
A024	HD 95418	13	6	ind.	ind.	2.2	24.455±0.096	Y	PI TI BE BM	
A028	HD 116657	18	15	ind.	52	1.2	26.309±0.579	?	SI LE	02 Mar
	13240+5456 A	35	36	ind.	ind.	1.0	25.064±0.088	?	SI	02 Mar
A029	HD 99211	32	17	ind.	ind.	1.9	25.246±0.127	N	LE	
A032	HD 103287	30	41	4.1	29.2	0.8	25.510±0.26	N	SI	22,23 Jan
A034	HD 165777	19	7	ind.	ind.	2.7	26.620±0.156	N	TI	
A035	HD 108767	28	29	ind.	ind.	1.0	26.637±0.113	N	BE	
A038	HD 18978	6	6	ind.	ind.	1.0	27.168±0.140	N	SC	
A039	HD 180777	4	10	ind.	ind.	0.4	27.303±0.142	N	LE	
A040	HD 33111	9	7	ind.	ind.	1.3	27.362±0.314	N	TI AP	
A041	HD 210418	9	7	ind.	ind.	1.3	28.180±0.671	N	TI PI BE	
A042	HD 87696	13	13	32	22	1.0	28.238±0.144	Y	SI PI BE	04 Dec
A045	HD 78209	107	77	119	19	1.4	28.818±0.208	N	SI	04 Dec
A048	HD 125161	24	28	ind.	52	0.9	29.067±0.161	N	SI	02 Mar
A049	HD 50241	12	8	ind.	ind.	1.5	29.398±1.528	N	TI	
A052	HD 159560	20	20	ind.	ind.	1.0	30.351±0.106	N	LE	
A053	HD 125162	14	8	21	22	1.8	30.355±0.147	Y	SI LE	02 Mar
A056	HD 56537	50	31	39	12	1.6	30.888±0.210	N	SI	08 Dec
A063	HD 222603	21	13	ind.	ind.	1.6	32.681±0.203	N	LE BE	
A064	HD 20320	53	21	ind.	ind.	2.5	33.650±0.328	Y	LE	
A065 ^e	15278+2906A	28	31	148	56	0.9	34.281±0.892	N	SI	02 Mar
A066	HD 104513	25	42	ind.	52	0.6	34.282±0.881	N	SI	22 Jan
A067	HD 14055	84	47	18	21	1.8	34.397±0.284	Y	SI	08 Dec
A068	HD 91312	29	40	122	19	0.7	34.627±0.623	?	SI	04 Dec

Table A1 – *continued* Polarization data for all the stars observed at OMM and from the Leroy compilation with a polarization $P < 3\sigma_P$.

UNS ID	name	P (10^{-5})	σ_P (10^{-5})	$\theta(^{\circ})$	$\sigma_{\theta} (^{\circ})$	P/σ_P	Distance (pc)	FIR ^a excess	Observer ^b	Date ^c
A069	HD 112412	24	13	109	22	1.8	36.900±5.523	?	SI LE	02 Mar
	HD 112413	31	42	ind.	ind.	0.7	35.247±1.093	?	SI	02 Mar
A074	HD 79439	124	71	60	16	1.7	35.837±0.257	N	SI	08 Dec
K077	HD 214749	22	23	ind.	ind.	1.0	36.367±0.528	N	SC	
A078	HD 184006	101	51	133	16	2.0	37.216±0.152	N	SI	02 Mar
A079	HD 102124	20	29	8	30	0.7	37.411±0.350	N	SI	02 Mar
A080	HD 177196	9	11	ind.	ind.	0.8	37.434±0.238	N	LE	
A082	HD 71155	0	43	ind.	52	0.0	37.514±0.267	Y	SI	22 Jan
A083	HD 80081	7	4	ind.	52	1.8	38.181±1.119	N	SI PI BE HA	21 Jan
A084	HD 78045	23	8	ind.	ind.	2.9	38.283±0.176	N	TI	
A086	HD 13161	46	24	ind.	52	1.9	38.865±0.514	Y	SI BE	23 Jan
A087	HD 95608	33	32	86	16	1.0	38.956±0.258	N	SI	23 Jan
A089	HD 215789	9	4	ind.	ind.	2.2	39.497±0.748	N	SC TI	
A090	HD 5448	34	12	ind.	ind.	2.8	39.602±1.341	N	TI BE	
A101	HD 130109	50	30	ind.	ind.	1.7	41.244±0.323	N	MA BE	
A103	HD 1404	18	29	ind.	ind.	0.6	41.291±0.358	Y	BE	
A104	HD 90132	70	30	ind.	ind.	2.3	41.477±0.464	N	MA	
A110	HD 89021	9	8	ind.	52	1.1	42.129±1.378	N	SI BE	22 Jan
A113	HD 23281	29	18	ind.	ind.	1.6	42.391±0.898	Y	LE	
A118	HD 15008	9	5	ind.	ind.	1.8	42.809±0.623	N	SC	
A123	HD 213398	14	6	ind.	ind.	2.3	43.804±0.422	Y	SC	
A127	HD 140436	28	29	ind.	52	1.0	44.621±1.010	N	SI BE	02 Mar
	HR 8799	70	25	95.5	8.9	2.8	39.4 ±0.1	Y	SI	08 Dec

^a Detection of FIR excess: yes (Y), no (N), no information or uncertain (?).

^b The key for the observers is the same as in Table 1.

^c Observations from OMM were obtained during the winter 2009-2010.

^d When the uncertainty on the polarization angle is larger than $\approx 52^{\circ}$, its orientation is indefinite (see section 3). Also it is customary not to give the polarization angle when the polarization is considered to be too small to yield a reliable polarization angle.

^e See the note about A065 in Table 1.